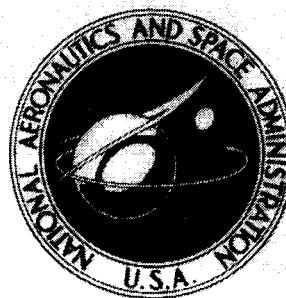


**NASA TECHNICAL
MEMORANDUM**



NASA TM X-1640

NASA TM X-1640

**CASE FILE
COPY**

**EFFECTS OF SEVERAL RAMP-FAIRING,
UMBILICAL, AND PAD CONFIGURATIONS
ON AERODYNAMIC HEATING TO
APOLLO COMMAND MODULE AT MACH 8**

by James L. Hunt and Robert A. Jones

Langley Research Center

Langley Station, Hampton, Va.

EFFECTS OF SEVERAL RAMP-FAIRING, UMBILICAL,
AND PAD CONFIGURATIONS ON AERODYNAMIC HEATING TO
APOLLO COMMAND MODULE AT MACH 8

By James L. Hunt and Robert A. Jones

Langley Research Center
Langley Station, Hampton, Va.

NATIONAL AERONAUTICS AND SPACE ADMINISTRATION

For sale by the Clearinghouse for Federal Scientific and Technical Information
Springfield, Virginia 22151 - CFSTI price \$3.00

EFFECTS OF SEVERAL RAMP-FAIRING, UMBILICAL,
AND PAD CONFIGURATIONS ON AERODYNAMIC HEATING TO
APOLLO COMMAND MODULE AT MACH 8

By James L. Hunt and Robert A. Jones
Langley Research Center

SUMMARY

An investigation was conducted in the Langley Mach 8 variable-density hypersonic tunnel to determine the effects of several ramp-fairing—protruding-leeward umbilical configurations with and without simulated wire bundle case, protruding shear pads, recessed shear and compression pads, and a recessed windward afterbody umbilical on heat transfer to the Apollo command module. Tests were made at angles of attack of 18° , 22° , and 26° and free-stream Reynolds numbers, based on model diameter, of 0.76×10^6 and 1.48×10^6 .

For the ramp-fairing—umbilical configurations tested in this investigation, the area of high interference heating on the body at the windward base of the leeward umbilical was reduced substantially below that which occurred for the configuration having a protruding leeward shear pad and a flush-face umbilical; however, no significant reduction in the peak interference heating factor was observed. The presence of a simulated wire bundle case on the windward face of the protruding leeward umbilical appeared to reduce the peak heating on the body at the base of the umbilical. The highest heating rates on the Apollo configurations tested occurred in the interference regions of the shear and compression pads. The magnitude of these interference heating rates was 3 to 4.5 times the stagnation-point value for an angle of attack of 22° and a free-stream Reynolds number of 0.76×10^6 based on model diameter. The placement of a recessed umbilical just downstream of the leading edge on the windward afterbody produced interference heating factors of 1.26 and 1.48 just downstream of the umbilical for Reynolds numbers of 0.76×10^6 and 1.48×10^6 , respectively. These heating factors were about 74 percent lower than the lowest peak factors obtained with any of the protruding leeward umbilical configurations.

INTRODUCTION

Wind-tunnel investigations on the effects of protuberances on heat transfer to the Apollo command module at an angle of attack of 33° and a Mach number of 8 (ref. 1)

indicated that the increases in heat transfer for the small region on the body immediately ahead of the leeward umbilical for a configuration having a protruding leeward shear pad, tension tie, protruding umbilical, and no wire bundle case may be as large as 8 to 10 times that for the smooth-body configuration at Reynolds numbers (based on body diameter and free-stream conditions) of 0.5×10^6 to 1.4×10^6 . Reference 2 gives heat-transfer increases 5 and 8 times that of the smooth body for this region at respective Reynolds numbers of 1.37×10^6 and 2.56×10^6 for the Apollo command module at an angle of attack of 33° and at a Mach number of 10.19. These large increases in heating were confirmed by the results of the orbital-velocity heat-shield qualification flight made in 1966. A photograph of the heat shield showing the erosion which occurred in the region ahead of the umbilical fairing during the qualification flight test is presented in figure 1.

In order to alleviate this "hot spot" which occurred in the earlier tests at $\alpha = 33^\circ$, two proposals were considered: (1) placing a ramp-fairing protuberance on the face of the module immediately ahead of the umbilical, centered along a streamline emerging at the stagnation point, and passing through the radial center line of the umbilical 1.895 centimeters from the axis of symmetry; (2) deleting the protruding umbilical on the leeward corner and placing a recessed umbilical on the windward afterbody.

Reference 1 obtained a value of 2 for the interference heating factor (defined as the ratio of the heat-transfer coefficient with interference to the heat-transfer coefficient at the same location on a smooth Apollo configuration) in the immediate downstream vicinity of the two protruding windward shear pads and a value of 1.3 for the protruding rearward shear pad. In order to reduce the interference heating which resulted from the protruding shear pads, recessed shear pads were proposed.

In cooperation with NASA Manned Spacecraft Center, an investigation was made in the Langley Mach 8 variable-density hypersonic tunnel to determine the heating rates to the surface of the ramp fairing and the interference heating rates to the surface of the vehicle in the vicinity of the fairing with emphasis on the region immediately ahead of the protruding leeward umbilical, the effect of the recessed windward afterbody umbilical on the aerodynamic heating to the windward afterbody, and the interference heating rates to the surface of the vehicle in the vicinity of the recessed shear and compression pads.

Eight different model configurations were tested. Many of the tests were made at an angle of attack of 22° and a Reynolds number based on the model diameter of 0.76×10^6 . However, tests were also conducted on some of these configurations at angles of attack of 18° and 26° and Reynolds numbers of 0.20×10^6 and 1.48×10^6 . The purpose of this paper is to present and discuss the results of this investigation.

SYMBOLS

c	specific heat of model material at constant pressure
c_p	specific heat of air at constant pressure
d	distance measured counterclockwise from left edge of ramp fairing along $s/R = 0.75$ grid line
D	maximum model diameter
h	aerodynamic heat-transfer coefficient
h_o	faired measured stagnation-point heat-transfer coefficient at angle of attack
h_s	calculated heat-transfer coefficient of stagnation point at an angle of attack of 0°
\bar{h}	interference heating factor (ratio of the heat-transfer coefficient with interference to the heat-transfer coefficient at the same location on a smooth model)
k	thermal conductivity of model material
l	heat penetration depth
$N_{Pr,w}$	Prandtl number at wall
r_c	corner radius (fig. 2)
r_n	nose radius (fig. 2)
R	maximum model radius
R_c	radial distance measured normal from axis of symmetry of model
$R_{\infty,D}$	Reynolds number based on model diameter and free-stream properties
s	surface distance measured from center of face (fig. 2)

t	time
t_d	thermal diffusion time
T_{aw}	adiabatic wall temperature
T_i	initial temperature of model
T_{pc}	temperature of phase change
\bar{T}	temperature parameter (eq. (2))
u	local velocity
w	width of unbeveled ramp
x_c	distance along axis of symmetry measured from center of face (fig. 3(a))
α	angle of attack
β	heat-transfer parameter (eq. (1))
θ_c	angular displacement measured clockwise about axis of symmetry, $\theta_c = 90^\circ$ at windward ray (fig. 5)
λ	thermal diffusivity, $k/\rho c$
μ_s	viscosity at stagnation conditions
μ_w	viscosity at wall
ρ	density of model material
ρ_s	density of air at stagnation conditions
ρ_w	density of air at wall conditions

FACILITY

All the data presented herein were obtained in the Langley Mach 8 variable-density hypersonic tunnel. This facility, which operates with air as the test media, has a contoured axisymmetric nozzle with a 37.72-centimeter-diameter test section. It is especially adapted for transient testing by means of a model injection mechanism located directly beneath the test section. Windows are located on both sides and the top of the test section for lighting and photographing the model. The nominal free-stream Mach numbers for the three Reynolds numbers ($R_{\infty, D} = 0.20 \times 10^6$, 0.76×10^6 , and 1.48×10^6) at which tests were conducted in this investigation are 7.65, 7.93, and 7.95, respectively.

MODELS

Eight different model configurations were used in this investigation. The main features of these models are listed in table I along with the figures in which detailed sketches of each model are shown.

TABLE I.- PRINCIPAL FEATURES OF TEST MODELS

[For all models, $D = 10.16$ cm, $r_n = 3.05$ cm]

Model	Figure	Afterbody angle, deg	Feature		
			Umbilical	Ramp fairing	Pads
1	2,3	35	Protruding leeward with wire bundle case	Two 5° approach slopes	Two protruding windward shear
2	4			One 10° approach slope	Two protruding windward shear
3	5,6			One 10° approach slope with beveled edges	Three shallowly recessed shear and three shallowly recessed compression
4	5,6,7			One 10° approach slope with beveled edges	Three deeply recessed shear and three deeply recessed compression
5	8	33	Protruding leeward with flush face	Two 5° approach slopes	None
6	9		Protruding leeward with flush face	None	One protruding leeward shear
7	10		Recessed, on most windward ray of afterbody just downstream of leading edge	None	None
8	10 (smooth)		None	None	None

Models 1 to 4 were obtained by successive modifications of an existing model. (See fig. 3 of ref. 1 for details of existing model.) These four models shown in detail in figures 2 to 7 represent the various ramp configurations, protruding windward shear pads, and recessed shear and compression pads tested. A rectangular protrusion was molded

to the windward face of the leeward umbilical on each of these models in an effort to simulate the wire bundle case present on the umbilical of the actual Apollo spacecraft.

The protruding leeward umbilical of models 5 and 6 differs from that of models 1 to 4 only in that it did not have a protuberance (wire bundle case) on the face of the umbilical. The umbilical for these two models was provided with a flush face so that more detailed photographs in this area could be made. Detailed photographs are essential to the technique used in obtaining the heat-transfer coefficients in this investigation. (The heat-transfer technique is described in the next section.) Model 5 (fig. 8) has a ramp fairing and protruding leeward umbilical, whereas model 6 (fig. 9) has a protruding leeward shear pad and protruding leeward umbilical. Note that the height of the protruding leeward shear pad on model 6 is 2.15 and 2.4 times that of the leeward shear pad on the models of references 1 and 2, respectively, which were used to investigate the high interference heating on the body at the base of the umbilical. Model 6 does not have a tension tie whereas the configurations of references 1 and 2 do. Models 5 and 6 were constructed as shown in order to compare more effectively the heating on the body at the base of the umbilical face for the ramp-fairing—umbilical configuration and for the shear-pad—umbilical configuration.

On model 7 (fig. 10), the protruding leeward umbilical was replaced by the recessed windward afterbody umbilical.

Model 8 was a smooth Apollo command module without any cavities or protuberances. The model in figure 10 without the recessed umbilical serves as the drawing for this configuration. For the smooth-body tests, two different models of this configuration were used. These models differed only in their thermophysical properties. One was used in conjunction with the face tests and the other with the afterbody tests. These two models are designated herein as model 8 (face) and model 8 (afterbody).

Throughout this report, models 1 to 6 and 8 (face) are referred to in a group as the face models whereas models 7 and 8 (afterbody) are referred to as the afterbody models.

TEST METHOD

Heat-transfer coefficients were obtained by using a phase-change-coating technique (ref. 3) which has been developed at the Langley Research Center to obtain quantitative heat-transfer data on complex shapes. This technique employs a coating of material which undergoes a visible phase change at a known temperature.

The time required for a phase change to occur at various locations on the model is determined by motion-picture photography. The patterns so obtained represent lines of constant surface temperature. These patterns also represent lines of constant

heat-transfer rate which, in principle, could be computed exactly from the general heat-conduction equation with the measured surface temperatures as boundary conditions applied to each test-body shape. Since the solution of this problem is not generally practical, the local heat transfer to the body is obtained from the solution for a semi-infinite slab.

Semi-Infinite Slab Solution

The value of the heat-transfer coefficient is obtained from solutions of the transient one-dimensional heat-conduction equation. A general form of the solution may be written as

$$h = \frac{\beta \sqrt{\rho c k}}{\sqrt{t}} \quad (1)$$

where h is the heat-transfer coefficient, $\rho c k$ is the product of the thermophysical properties of the model, t is the time required for a phase change to occur relative to the time the model is subjected to the tunnel free-stream conditions, and β depends only on the parameter

$$\bar{T} = \frac{T_{pc} - T_i}{T_{aw} - T_i} \quad (2)$$

The functional dependence of β on \bar{T} is given in reference 3. A detailed description of this technique and solutions of the one-dimensional heat-conduction equation with initial and boundary conditions which most nearly describe the actual transient tests are available in references 1 and 3.

The results obtained from the semi-infinite slab assumption are a good approximation to the solution for actual body geometry when the depth of heat penetration is small compared with pertinent model dimensions. The depth of heat penetration for the semi-infinite slab is approximately independent of aerodynamic heat-transfer coefficient and depends only on the thermal diffusivity of the wall and the thermal diffusion time. A conservative approximation of the heat penetration depth l is given in the notation of the present paper by the following equation from reference 3

$$l = \sqrt{\frac{\lambda t_d}{0.2}} \quad (3)$$

Since the general heat-conduction equation is linear, equation (3) can be used to estimate the minimum distance from a protuberance (corresponding to an abrupt change in heating rate or model configuration) where the semi-infinite slab assumption is still valid.

Substitution of the time required for the phase change to occur from equation (1) for the thermal diffusion time t_d in equation (3) gives

$$l = \frac{\beta k}{\sqrt{0.2h}} \quad (4)$$

The value of l from this equation then gives the minimum distance of approach to a surface discontinuity where a semi-infinite slab solution can be used as a good approximation; however, for this semi-infinite slab solution to be accurate, the radius of body curvature must be much greater than the heat penetration depth. The distance l/w is plotted in figure 11 for the various test conditions and phase-change temperatures encountered in this investigation which required the determination of heat-transfer coefficients close to cavities or protuberances. How accurate the semi-infinite slab assumption is inside the minimum distance of approach is not known. The large separation of the two sets of curves in figure 11 is due to the difference in the thermal conductivity of the face and afterbody models.

Thermophysical Properties of Models

The thermophysical properties (specific heat, thermal conductivity, and density) were measured on samples of the model material by a private corporation under contract with Langley. Measurements made at Langley after the testing of the face configurations (models 1 to 6 and model 8(face)) indicated that the thermal conductivity of this plastic material may vary as much as 50 percent depending on the curing time and orientation of the sample during the curing process. Since, at the time the plastic material for these face models was made, no consistent curing procedure to insure accurate properties was followed, the thermophysical properties of this material were questionable.

The product term ρck which is needed for the present technique was evaluated for each of the face models by using heat-transfer coefficients obtained in the Mach 8 variable-density hypersonic tunnel by means of the thin-skin calorimeter transient testing technique on a smooth, thermocouple-instrumented, Apollo model (ref. 4). Only the heat-transfer coefficients at the geometric centers of the models (taken from cross plots of the smooth-body data presented in ref. 4 to insure matching with the present data of both angle of attack and Reynolds number) were utilized in this evaluation. Since the heat-transfer coefficient is essentially independent of model surface temperature, for given test conditions, the ρck term can then be evaluated directly from equation (1) by inserting the independently determined values of h and the observed values of t and β from the present tests. The derived value of $\sqrt{\rho ck}$ for each of the face models is given in table II.

TABLE II. - COMBINED THERMOPHYSICAL PROPERTIES OF MODELS

Model	$T_{pc},$ °K	$\sqrt{\rho ck},$ $W\sqrt{sec}/m^2-^{\circ}K$
1,2,3,4	394	1.68×10^3
1,2,3,4	450	1.86
5	394	1.72
6	394	1.88
8 (face)	394	1.80

The maximum variation in $\sqrt{\rho ck}$ for these models is seen to be about 10 percent which is well within the accuracy of conventional methods used to measure these properties.

At the time the afterbody configurations (models 7 and 8 (afterbody)) were made, a curing procedure which utilized an accelerating agent had been established that supposedly would produce specimens of this plastic material with consistent thermophysical properties. Measurements made at Langley on such a specimen gave an average value of $1.31 \times 10^3 W\sqrt{sec}/m^2-^{\circ}K$ for $\sqrt{\rho ck}$ over a temperature range from $311^{\circ} K$ to $366^{\circ} K$. This value of $\sqrt{\rho ck}$ was used for models 7 and 8 (afterbody) coatings having phase-change temperatures of $316^{\circ} K$ and $333^{\circ} K$. Application of the procedure used previously in determining $\sqrt{\rho ck}$ for the face models to the tests of models 7 and 8 (afterbody) gave the same value of $\sqrt{\rho ck}$ for these models as was measured directly. Heat-transfer coefficients along the windward ray taken from cross plots of afterbody data presented in reference 5 were used in this calculation.

PRESENTATION FORM AND INTERPRETATION OF FIGURES

The heat-transfer data are presented both in terms of the nondimensional heat-transfer ratio h/h_s and the interference heating factor \bar{h} . The reference values of h_s (stagnation-point heat-transfer coefficient for $\alpha = 0^{\circ}$) were calculated by the following equation from reference 6, given in terms of the present paper

$$h_s = 0.768c_p(N_{Pr,w})^{-0.6}(\rho_w\mu_w)^{0.1}(\rho_s\mu_s)^{0.4}\left(\frac{du}{ds}\right)^{0.5} \quad (5)$$

where du/ds was determined by multiplying the Newtonian velocity gradient of a sphere of radius r_n by 1.19 (ref. 5).

The calculated variation of h_s with Reynolds number is plotted in figure 12. Measured values from reference 4 are shown for comparison. The reason for the discrepancy

between computed and measured values is not known; however, the difference shown appears to be typical of wind-tunnel data as shown by Bertin (ref. 7). Figure 12 is presented to emphasize the increase in deviation of the calculated and measured heat-transfer coefficients with increasing Reynolds number. Whether similar deviations in values of h away from the stagnation point might occur is not known.

Since most of the conclusions drawn from this investigation are based on relative comparisons, the results are presented as matched sequences of photographs and isothermal contours sketched from photographs of the phase-change patterns. The various combinations of models and test conditions investigated along with the respective figure numbers of the corresponding h/h_s contour sketches and photographic sequences are presented in table III. For all photographs and sketches presented in this report, the flow is from bottom to top so that the stagnation point is located near the bottom of each picture along the vertical center line of the model. The figures show a distorted view of the surface because of the angle between the camera and model.

TABLE III.- COMBINATIONS OF MODELS AND TEST CONDITIONS INVESTIGATED

Model	Region of interest	Test conditions for contour sketches		h/h_s contour figures	Test conditions for photo sequences		Photo-sequence figures
		$R_{\infty,D}$	α , deg		$R_{\infty,D}$	α , deg	
1	Face	-----	---	---	0.76×10^6	26	23
2	Face	0.76×10^6	22	14	.76	18,22	19
3	Face	.76	22	15	.76	18,22,26	20
4	Face	.76	22	16	.76	18,22,26	21
5	Face	.76	22	17	.76	22	} 22
6	Face	.76	22	18	.76	22	
7	Afterbody	{ .76 1.48	} 22	27			
8	Face	.76	22	13			
8	Afterbody	{ .20 .76 1.48	} 22	25			

Figure 13 shows the heat-transfer-coefficient contours for the smooth-body model traced from photographs of tests conducted on the face of model 8 at a Reynolds number of 0.76×10^6 and an angle of attack of 22° . The stagnation point is indicated by an encircled cross on the $\theta_c = 90^\circ$ line at s/R of approximately 0.6. The location and value

of the heat-transfer coefficient at this point was obtained from cross plots of the data presented in reference 4. Since this test condition was the only one at which data were obtained on the smooth-body face, it is the only test condition for which interference heating factors are presented.

Sketches of heat-transfer coefficient ratios are presented in figures 14 to 18 for models 2 to 6, respectively, for a Reynolds number of 0.76×10^6 and an angle of attack of 22° only. The contours shown in these figures and in figure 13 were traced from a projection onto a screen of a 35-millimeter negative taken during actual tunnel tests. In order to locate the phase-change patterns (heat-transfer-coefficient contours) accurately, photographs of a grid model located in the identical position in the test section as that of the test model were superimposed on all sketches. The broken contour lines in the sketches indicate uncertainty in phase-change—interface position. Since the emphasis herein is on or near the cavities and protuberances (note that the broken lines appear on the smooth portion of the model), no additional tests using phase-change temperature coating that would give distinct phase-change pattern on the smooth portion of the model were made. The contours of h/h_S are shown in the (a) part of figures 14 to 18. In the (b) part of these figures, the value of \bar{h} is given at certain points designated by crosses. The lines of constant h/h_S are repeated for convenience.

Figures 19 to 23 give samples of the actual photographs taken during the tests and are presented in various sequences to illustrate the effects of all the test variations included in this investigation on models 1 to 6. Thus, qualitative comparison of the effects of angle of attack and Reynolds number for the various configurations tested can be made. The light areas in the photographs of these figures are areas in which the phase change has already occurred and consequently represent regions of higher heat-transfer rates than the dark areas. These photographs were taken by a polaroid camera directly off the screen from the negative film projections.

The photographs arranged in any given column in these figures are sequences of phase-change patterns for a given test and thus represent different test times, and the contours represent different heating rates.

In figures 19 to 23 there are six rows of photographs designated (a) to (f) with an h/h_S value corresponding to the line separating the light and dark areas in the photographs given for each row. In these figures the h/h_S value is the same for any given row. Thus, the relative effect of geometry, angle of attack, and Reynolds number on the interference heating produced by a given cavity or protuberance can be determined by comparing the phase-change areas in the photographs of the pertinent rows or columns of the various figures. Such a comparison should be made before concluding that a given configuration produces less interference heating than another since the given h/h_S value

only applies to the interface and not the areas where the phase change has already occurred. (The areas where the phase change has occurred have heating rates higher than those designated for the interface.)

RESULTS AND DISCUSSION

Interference Heating to Body Immediately Ahead of Protruding Leeward Umbilical

In order to obtain some indication of the efficiency of the various ramp-fairing configurations which were designed to alleviate the high interference heating occurring just upstream of the umbilical face on a model without a ramp (model 6, fig. 18), a comparison was made of the data in figures 14 to 18. These figures show the heat-transfer-coefficient contours and interference heating factors for the various ramp configurations at $R_{\infty,D} = 0.76 \times 10^6$ and $\alpha = 22^\circ$. Figure 14(b) shows the highest interference heating factors on the body to be at the front base of the umbilical for the unbeveled smooth ramp-fairing configuration (model 2) and to be 4.5 and 4.7 at the right and left sides, respectively (right is clockwise to the center line of the umbilical ($\theta_c = 286.1^\circ$, fig. 2) and left is counterclockwise as viewed normal to the face in figs. 14 to 23). For model 3, having shallowly recessed shear pads, and a beveled ramp fairing, the highest interference heating factor is 6 but occurs only at the left front side of the umbilical. (See fig. 15(b).) For model 4, having deeply recessed compression pads, and a beveled ramp fairing, the interference heating factors on the body at the left and right side of the umbilical face are 6.0 and 4.7, respectively. (See fig. 16(b).) On the basis of the peak interference heating factors at the base of the umbilical, the wider unbeveled ramp (model 2) is more effective than its beveled counterparts (models 3 and 4). Also, of the two beveled ramps, the region of high interference heating at the base of the umbilical is less extensive for the ramp with the shallowly recessed shear pad (model 3). For model 5, having a flush-face umbilical and an unbeveled ramp fairing, the highest interference heating factor is 10 and occurs at the right side of the umbilical face (fig. 17(b)). Note that the peak interference heating factor is significantly less for the various ramp-fairing—umbilical configurations which have a protrusion (wire bundle case) on the windward face of the umbilical than for that without a protrusion (model 5). Figure 18(b) shows interference heating factors for model 6, having a flush-face umbilical and a protruding shear pad. The highest interference heating factor at the base of the umbilical shown here is 4.8 for an angle of attack of 22° . The peak interference heating factors that occur on the body at the base of the umbilical and the corresponding ratio of heat-transfer coefficient to stagnation-point heat-transfer coefficient for $\alpha = 22^\circ$ and $R_{\infty,D} = 0.76 \times 10^6$ are given in table IV:

TABLE IV.- INTERFERENCE HEATING AT THE WINDWARD BASE
OF THE PROTRUDING LEEWARD UMBILICAL

Model	Ramp-umbilical description	Peak \bar{h} shown	h/h_o at $\alpha = 22^\circ$
2	Unbeveled ramp, no pad, wire bundle case	4.7	0.93
3	Beveled ramp, shallowly recessed pad, wire bundle case	6.0	1.195
4	Beveled ramp, deeply recessed pad, wire bundle case	6.0	1.195
5	Unbeveled ramp, no pad, flush-face umbilical	10	1.57
6	No ramp, protruding shear pad, flush-face umbilical	4.8	.93

Comparison of the peak interference heating factor at the base of the umbilical face at $\alpha = 22^\circ$ and $R_{\infty, D} = 0.76 \times 10^6$ of the various configurations indicated that the presence of the ramp fairing caused no significant reduction in peak interference heating over that which occurred for the protruding leeward shear pad-umbilical configurations of this report. However, the total effectiveness of the ramp-fairing configurations also depends on the extent of the area where high interference heating occurs. An examination of this area can best be made by comparing the phase-change patterns of the photographs for $\alpha = 22^\circ$ in the (e) and (f) parts of figures 19 to 22. These parts show interface lines representing heat-transfer-coefficient ratios h/h_s of 0.83 and 0.70, respectively.

A comparison of the interference heating of model 2, having an unbeveled smooth ramp and no pads (figs. 19(e) and 19(f)), and model 6, having no ramp and a protruding shear pad (figs. 22(e) and 22(f)), indicates that the interference heating of model 2 is confined to a smaller area in front of the umbilical than that of model 6. For model 3 with the shallowly recessed shear pads (figs. 20(e) and 20(f)) and model 4 with the deeply recessed shear pads (figs. 21(e) and 21(f)), the interface heating is confined to the front left corner of the umbilical face directly behind the recessed shear pad. For both of these models, there is a significant reduction in the interference heating area on the body at the windward base of the umbilical over that which occurred for model 6, having a protruding shear pad, in figures 22(e) and 22(f). For model 5, having a smooth ramp fairing and a flush-face umbilical, the interference heating area occurs extensively on the body at both corners of the umbilical face but is much more predominant at the right corner. (See figs. 22(e) and 22(f).) In models 2 to 4 where the wire bundle case is

simulated, the interference heating area on the body at the base of the windward corners of the umbilical is significantly less extensive than that which occurs with model 5, having a flush-face umbilical and no wire bundle case. The interference heating area that occurs at the base of the umbilical on model 5, having a ramp fairing, is less than that which occurs on model 6, having no ramp fairing. (See figs. 22(d) to 22(f).)

The preceding observations are summarized as follows:

The peak interference heating factor on the body at the base of the umbilical for model 6, a protruding leeward shear-pad—umbilical configuration (no ramp, no simulated wire bundle, no tension tie) was 4.8 at $\alpha = 22^\circ$ and $R_{\infty, D} = 0.76 \times 10^6$. Reference 1 reports that this factor may be as high as 8 to 10 at $\alpha = 33^\circ$ for a configuration having a protruding leeward shear pad which was about one-half the height of those herein, tension tie, protruding umbilical, and no wire bundle case.

The peak interference heating factors on the bodies of models 2 to 4 at the windward base of the leeward umbilical on which the simulated wire bundle case appeared were significantly less (4.7 to 6.0 compared with 10) than occurred on model 5, having no wire bundle case, at an angle of attack of 22° .

For models 2 to 4, having a ramp fairing, protruding leeward umbilical, and simulated wire bundle case, the peak interference heating factor which occurred on the body at the base of the umbilical was smallest (4.7 compared with 6.0) for model 2, having a wider unbeveled ramp. In addition, the peak interference heating factors for models 2 to 4 were not significantly reduced (4.7 to 6 compared with 4.8) below that which occurred with the protruding leeward shear-pad—umbilical configuration (model 6). The area of high interference heating at the windward base of the leeward umbilical for these models was reduced substantially below that which occurred for protruding leeward shear-pad—umbilical configuration (model 6).

The preceding observations also indicate that the interference heating on the body at the base of the umbilical is very sensitive to the alinement, width, and height of the ramp fairing. Differences in these features for each model may have been caused by difficulty in alining each ramp, the use of different molds for the ramp fairing on model 5 and model 1, modification of the ramp fairing on model 1 for use on models 2, 3, and 4, and unequal removal of material from the ramp in the beveling process. The interference heating is also very sensitive to the presence of a cavity on the ramp and to the presence of a wire bundle case.

The effect of angle of attack on the interference heating to the body immediately ahead of the umbilical face for three of the ramp-fairing configurations (models 2, 3, and 4) may be seen in figures 19, 20, and 21, respectively, by comparing the area over which the phase-change has occurred for the same models and same h/h_s values at

angles of attack of 18° , 22° , and 26° . For each of these models, the interference heating area decreases with increasing angle of attack.

The effect of Reynolds number on the interference heating to the body immediately ahead of the umbilical face for model 1, having a smooth unbeveled ramp, (only ramp configuration tested at a Reynolds number other than 0.76×10^6) may be seen in the photographs of figure 23. Comparison of the phase-change area at the base of the umbilical for the same h/h_s value at Reynolds numbers of 0.76×10^6 and 1.48×10^6 (figs. 23(e) and 23(f)) indicates that the interference heating to the body immediately ahead of the umbilical face in terms of h/h_s increases for increasing Reynolds number.

All the heat-transfer-coefficient ratios given in figures 14 to 23 for the region immediately ahead of the protruding leeward umbilical are located within the minimum distance of approach, as given in figure 11, to either the umbilical or the ramp's stern. Consequently, as discussed herein, the validity of the semi-infinite slab solution in this particular area is questionable. However, the general conclusions concerning this region should not be affected since these conclusions are of a comparative nature and therefore depend mainly on the qualitative aspects of the technique rather than the quantitative results.

Interference Heating to Body Along Edges of Ramp

The effects of ramp geometry, angle of attack, and Reynolds number on the interference heating to the body along the sides of the ramp and the heating which the face of the ramp incurs is discussed herein. Three basic ramp-fairing configurations were tested in this investigation: type 1 had an unbeveled edge with one 10° slope into the face of the body (model 2, fig. 4); type 2 had a beveled edge with one 10° slope into the face of the body (models 3 and 4, fig. 6); type 3 had an unbeveled edge with two 5° slopes into the face of the body (models 1 and 5, figs. 3 and 8, respectively). The interference heating on the body along the edges of each ramp type in terms of interference heating factors can be seen in figures 14(b), 16(b), and 17(b), respectively, for a Reynolds number of 0.76×10^6 and an angle of attack of 22° .

The peak interference heating factor on the body at the left edge of the ramp at an s/R position of 0.75 is approximately 2.0, 1.6, and 2.0 for the respective ramp types.

The peak interference heating factor on the body in the region of the left leeward corner of the ramp ($0.99 < s/R < 1.04$) is given in figures 14(b), 16(b), and 17(b) as 2.7, 2.3, and 2.3 for the respective ramp types. The interference factors in this particular region are not accurate because the s/R values here could not be determined with any accuracy. Also the phase-change area in this region shown in the photographs of figures 19 to 22 is not very distinct; therefore, no conclusions concerning the interference

heating of a given ramp type compared with another are made in this region. However, comparison of the phase-change area along the sides of the ramps at the same value of h/h_s in figures 19 to 22 does show that the interference heating is less for the beveled ramp (type 2) and increases as the angle of attack decreases for all three ramp types. (Ramp type 3 was tested only at $\alpha = 22^\circ$, but the same trend should hold.)

Comparison of the phase-change area for the same h/h_s value on the sloping portion of the ramp face at $\alpha = 22^\circ$ for ramp type 1 of model 2 in figure 19, ramp type 2 of models 3 and 4 in figures 20 and 21, and ramp type 3 of model 5 in figure 22 shows that the interference heating on the sloping portion of the ramp is less for the ramp with two 5° slopes into the face of the body (type 3) than those with one 10° slope into the face of the body (types 1 and 2). By the same comparison, from figures 19 and 22, it is evident that the interference heating is also less for the flat portion of the type 3 ramp provided no cavities exist in this region.

For the type 3 ramp (unbeveled – two 5° slopes into the face of the body) of model 1, which was the only ramp tested at two free-stream Reynolds numbers, the effect of Reynolds number on the interference heating to the sides and face of the ramp can be seen by comparing the area over which the phase change has occurred for the same h/h_s value at Reynolds numbers of 0.76×10^6 and 1.48×10^6 in figure 23. The peak interference heating on the body very close to and along the left side of the ramp in terms of h/h_s is largest for the lower Reynolds number. (See figs. 23(b) to 23(d).) However, as the perpendicular distance from the edge of the ramp increases, the interference heating decreases more rapidly at the lower Reynolds number than at the higher one. (See figs. 23(e) and 23(f).) The heat-transfer-coefficient ratio h/h_s is plotted as a function of d/w (the distance measured counterclockwise from the left edge of the ramp along the $s/R = 0.75$ grid line divided by the width of the ramp) in figure 24; this figure shows that the heat-transfer-coefficient ratios for the $R_{\infty,D} = 1.48 \times 10^6$ test were higher than those for the $R_{\infty,D} = 0.76 \times 10^6$ test for d/w greater than approximately 0.25.

Comparison of the phase-change area on the face of the ramp for the two different Reynolds number tests presented in figures 23(a) to 23(d) shows the interference heating to this region in terms of h/h_s to be essentially independent of this Reynolds number range; however, figure 23(e) indicates that there is a small region in the center of the flat face portion of the ramp where the interference heating in terms of h/h_s increases with Reynolds number.

Interference Heating to Body in Vicinity of Shear and Compression Pads

Four pad configurations were tested in this investigation, two protruding windward shear pads on models 1 and 2 (fig. 2), one protruding leeward shear pad on model 6 (fig. 9), six shallowly recessed shear and compression pads on model 3, and six deeply

recessed shear and compression pads on model 4 (fig. 5). Table V gives the peak interference-heating factors shown for the various pad configurations in figures 14(b), 15(b), 16(b), and 18(b) along with the corresponding ratios of heat-transfer coefficients to the stagnation-point value for $\alpha = 22^\circ$ and $R_{\infty,D} = 0.76 \times 10^6$.

TABLE V.- INTERFERENCE HEATING IN THE VICINITY OF
SHEAR AND COMPRESSION PADS

Pad description	Pad position (fig. 5)	Peak \bar{h} shown	h/h_o at $\alpha = 22^\circ$	Model
Protruding windward shear pad	1	2.4	2.4	1,2
Shallowly recessed shear pad	1	2.3	2.4	3
Deeply recessed shear pad	1	2.3	2.4	4
Shallowly recessed compression pad	2	1.3	1.6	3
Deeply recessed compression pad	2	2.2	2.4	4
Protruding windward shear pad	3	2.5	2.4	1,2
Shallowly recessed shear pad	3	2.4	2.4	3
Deeply recessed shear pad	3	2.4	2.4	4
Shallowly recessed compression pad	4	3.8	2.4	3
Deeply recessed compression pad	4	3.8	2.4	4
Protruding leeward shear pad	5	4.7	2.4	6
Shallowly recessed leeward shear pad	5	4.1	2.4	3
Deeply recessed leeward shear pad	5	4.1	2.4	4
Shallowly recessed compression pad	6	3.5	2.4	3
Deeply recessed compression pad	6	3.5	2.4	4

Note that the peak values of \bar{h} for the region ahead of the umbilical given in table II are 2 to 3 times the value of those listed in table V for the shear and compression pads whereas the ratio of the heat-transfer coefficient to the stagnation-point value is a factor of 2 to 3 times less than the corresponding ratios listed for the shear and compression pads. Thus, the highest heating rates on the Apollo configuration occur in the vicinity of the shear and compression pads and not at the base of the umbilical where the highest peak interference heating factors are experienced. These maximum heating rates are 3 to 4.5 times the stagnation-point value at $\alpha = 22^\circ$ and $R_{\infty,D} = 0.76 \times 10^6$. This same magnitude of maximum heating rate was also observed on the windward face of the leeward umbilical with and without the wire bundle case. The highest h/h_s contour shown in both the sketches and photographs is 3.06 which corresponds to the local stagnation-point heat-transfer ratio of 2.4 in table V. The h/h_s contours of 3.06 enclose an appreciable area on the leeward side of the shear and compression pads and on the windward

face of the leeward umbilical. (See figs. 14 to 21.) The h/h_s contours on the umbilical face in the sketches of figures 14 to 16 were omitted because of the intricate detail involved. Phase changes corresponding to h/h_s values of 5 were observed to occur in the areas enclosed by the h/h_s contours of 3.06 in less than a quarter of a second after injection of model into the tunnel stream. For observation times of this order, errors of 20 to 30 percent are to be expected (see ref. 3); therefore, the maximum heating rate is bracketed between 3 and 4.5 times that of the stagnation-point value.

Since the deviation of the peak interference heating factors among members of a given "pad group," that is, same pad position but different pad configuration, is within the error band of the factors themselves except for pad groups 2 and 5, the area enclosed by a given h/h_s ratio contour in the vicinity of the pads is used as a means of comparing the various configurations among the given pad groups. This type of comparison can best be made from figures 19 to 23.

A comparison of the phase-change area on the face of the model in the downstream vicinity of the protruding windward shear pads in the photographs of figure 19 with the phase-change area in the vicinity of the shallowly and deeply recessed shear pads in positions 1 and 3 in the photographs of figures 20 and 21, respectively, for the same h/h_s value indicates that the interference heating in terms of h/h_s is: (1) less for the shallowly recessed shear pads than for both the protruding and deeply recessed shear pads, (2) approximately the same for the protruding shear pads and the deeply recessed shear pads, (3) increasing for decreasing angles of attack for the deeply recessed shear pads, and (4) approximately independent of the angle-of-attack range for the protruding shear pads and the shallowly recessed shear pads.

A comparison of the phase-change area on the face in the immediate vicinity of the shallowly and deeply recessed compression pad in position 2 of figures 20 and 21, respectively, for the same h/h_s value indicates that the interference heating in terms of h/h_s is less for the shallowly recessed compression pad than for the deeply recessed compression pad and is approximately independent of the angle-of-attack range.

A comparison of the phase-change areas on the face of the model in the immediate vicinity of the shallowly and deeply recessed compression pads in positions 4 and 6 in the photographs of figures 20 and 21, respectively, for the same h/h_s value indicates that the interference heating in terms of h/h_s is less for the shallowly recessed compression pads than for the deeply recessed compression pads and increases for decreasing angle of attack for both depths.

Since pad group 5 consists of a shallowly and a deeply recessed shear pad on the face of the ramp of models 3 and 4, respectively, and a protruding shear pad located at approximately the same s/R and angular location as on the command module with no ramp, only the two pads (shallow and deep) on the ramp can be effectively compared with

each other. Comparison of the phase-change areas on the ramp in the vicinity of shallowly and deeply recessed shear pads in position 5 in the photographs of figures 20 and 21, respectively, for the same h/h_s values indicates that the interference heating in terms of h/h_s is less for the shallowly recessed shear pad than for the deeply recessed shear pad and increases for decreasing angles of attack for both depths.

For the protruding shear pad in position 5 on model 6, the interference heating on the body in the vicinity of this pad is greater than that which occurs on the ramp due to either the shallowly or deeply recessed shear pad. (Compare figs. 20, 21, and 22 at $\alpha = 22^\circ$ for the same h/h_s values.)

For the protruding windward shear pads in positions 1 and 3 which were the only pad configurations tested at Reynolds numbers of 0.76×10^6 and 1.48×10^6 , the interference heating in terms of h/h_s increases slightly with increasing Reynolds number for this test range. This increase can be seen by comparing the phase-change areas in the vicinity of these pads for the same h/h_s value but different Reynolds number in the photographs of figures 23(a) to 23(c).

Effects of Recessed Windward Umbilical on Windward Afterbody Heating

Smooth windward afterbody heating. - The heat-transfer-coefficient-ratio contours for the smooth windward afterbody on model 8 for an angle of attack of 22° and Reynolds numbers of 0.20×10^6 , 0.76×10^6 , and 1.48×10^6 are given in figures 25(a), 25(b), and 25(c), respectively. The heat-transfer-coefficient ratio along the most windward ray ($\theta_c = 90^\circ$) is plotted against s/R in figure 26.

The level of the data in terms of h/h_s as shown in figure 26 is essentially the same for each of the three Reynolds number tests. An expected initial decrease occurs immediately downstream of the leading edge and then the data levels off at an s/R position of 1.4. The level remains constant until an s/R position of approximately 1.75 is reached. Here the level of the data for each of the three Reynolds numbers begins to increase significantly until a peak value is reached at an s/R position of 2.09. Then a decrease occurs which is probably due to heat conduction into the stainless-steel sting supporting the model. Therefore, only the rise which begins at an s/R position of 1.75 is discussed. Transition seems to have been eliminated since the rise in the level of data for each Reynolds number tested occurred at essentially the same position. Tests in which an excessive amount of phase-change coating was applied to the model so that on melting, the coating flowed in the local stream direction indicated that the flow is attached for the three Reynolds numbers. Therefore, one possible explanation for this rise in heat-transfer coefficient is that the afterbody radius is decreasing with increasing values of s/R and is producing cross-flow velocity gradients along and near the most

windward ray that increase with s/R . This phenomena does not occur further upstream because of the dominance of the leading-edge effect.

Windward afterbody heating with recessed umbilical. - The heat-transfer-coefficient-ratio contours for the windward afterbody of model 7 (recessed windward umbilical configuration) for an angle of attack of 22° and Reynolds numbers of 0.76×10^6 and 1.48×10^6 are given in figures 27(a) and 27(b), respectively. The heat-transfer-coefficient ratios along the most windward ray ($\theta_c = 90^\circ$) for this configuration are plotted against s/R in figure 28. The trend for these data is essentially the same as that for the smooth-body data insofar as the decrease immediately downstream of the leading edge and the increase at an s/R of 1.75 is concerned.

The interference heating factors for both Reynolds number tests (0.76×10^6 and 1.48×10^6) along the most windward ray of model 7 ($\theta_c = 90^\circ$) are given as a function of s/R in figure 29. The interference heating factors on the recessed umbilical floor range from approximately 0.81 to 0.96 over the length of the umbilical ($s/R = 1.2$ to 1.322) and seem to be independent of Reynolds number. Immediately downstream of the recessed umbilical, the interference heating factors abruptly increase to 1.26 and 1.48 for Reynolds numbers of 0.76×10^6 and 1.48×10^6 , respectively. This increase in the interference heating factor is transmitted over the afterbody and is more prominent for the higher Reynolds number test. (See fig. 29.) However, these heating factors were about 74 percent lower than the lowest peak factors obtained with any of the protruding leeward umbilical configurations.

CONCLUSIONS

The results of this experimental investigation on the effects of several ramp fairing, umbilical, and pad configurations on the aerodynamic heating to the Apollo command module at a Mach number of 8 and angles of attack from 18° to 26° indicate:

Ramp-Fairing—Protruding Leeward Umbilical Configuration

1. The interference heating rate and the interference heating area on the body at the base of the protruding leeward umbilical for the configurations having a ramp were highly sensitive to the alinement of the ramp, to the presence of a recessed shear pad on the ramp, and the presence of a simulated wire bundle case.

2. For the ramp-fairing—umbilical configurations tested on which the wire bundle case was simulated, the peak interference heating factors on the body at the base of the protruding leeward umbilical were not significantly reduced below that which occurred for the protruding leeward shear-pad and flush-face umbilical configuration (no tension

tie, no wire bundle case). For an angle of attack of 22° and a Reynolds number of 0.76×10^6 , these peak interference heating factors varied from 4.7 to 6.

3. For the ramp-fairing—umbilical configurations tested, the area of high interference heating on the body at the windward base of the leeward umbilical was reduced substantially below that which occurred for the configuration having a protruding leeward shear pad and a flush-face umbilical.

4. The area of interference heating at the base of the umbilical in the presence of a ramp increased with decreasing angle of attack and increased with increasing Reynolds number.

5. The presence of a simulated wire bundle case located on the windward face of the protruding leeward umbilical appeared to reduce the peak heating on the body at the base of the umbilical.

6. The interference heating on the face of the command module along the edges of the ramp was less for configurations in which the edges of the ramp were beveled. It also decreased with increasing angle of attack.

7. The results obtained by beveling the edges of the ramp indicated that a ramp wider than the ones tested may possibly give a further reduction in interference heating factor on the body at the base of the umbilical.

8. The interference heating on the base of the ramp was less for ramps whose profiles contained two 5° slopes than for those with one 10° slope.

Shear and Compression Pads

1. The highest heating rates on the Apollo configurations tested occurred in the interference regions of the shear and compression pads. For an angle of attack of 22° and free-stream Reynolds number based on face diameter of 0.76×10^6 , these heating rates were 3 to 4.5 times the stagnation-point value at zero angle of attack.

2. The interference heating rates to the body in the vicinity of the recessed shear and compression pads increased with an increase in the depth of the pad and decreased for increasing angle of attack.

3. The interference heating rate to the body in the vicinity of the protruding windward shear pads is approximately of the same magnitude and distribution as that for their deeply recessed counterparts.

Recessed Umbilical

1. The placement of a recessed umbilical just downstream of the leading edge on the windward afterbody produced interference heating rates about 26 and 48 percent above the smooth-body values for Reynolds numbers of 0.76 and 1.48×10^6 , respectively.

2. The interference heating factors on the recessed umbilical floor range from approximately 0.81 to 0.96 over the length of the umbilical (ratio of surface distance to radius s/R being 1.2 to 1.322) and seem to be independent of Reynolds number.

Langley Research Center,
National Aeronautics and Space Administration,
Langley Station, Hampton, Va., May 28, 1968,
129-01-03-07-23.

REFERENCES

1. Jones, Robert A.; and Hunt, James L.: Effects of Cavities, Protuberances, and Reaction-Control Jets on Heat Transfer to the Apollo Command Module. NASA TM X-1063, 1965.
2. Bertin, John L.: The Effect of Protuberances, Cavities, and Angle of Attack on the Wind-Tunnel Pressure and Heat-Transfer Distribution for the Apollo Command Module. NASA TM X-1243, 1966.
3. Jones, Robert A.; and Hunt, James L.: Use of Fusible Temperature Indicators for Obtaining Quantitative Aerodynamic Heat-Transfer Data. NASA TR R-230, 1966.
4. Jones, Robert A.: Measured Heat-Transfer and Pressure Distributions on the Apollo Face at a Mach Number of 8 and Estimates for Flight Conditions. NASA TM X-919, 1964.
5. Jones, Robert A.: Experimental Investigation of the Overall Pressure Distribution, Flow Field, and Afterbody Heat-Transfer Distribution of an Apollo Reentry Configuration at a Mach Number of 8. NASA TM X-813, 1963.
6. Fay, J. A.; and Riddell, F. R.: Theory of Stagnation Point Heat Transfer in Dissociated Air. J. Aeronaut. Sci., vol. 25, no. 2, Feb. 1958, pp. 73-85, 121.
7. Bertin, John J.: Wind-Tunnel Heating Rates for the Apollo Spacecraft. NASA TM X-1033, 1965.

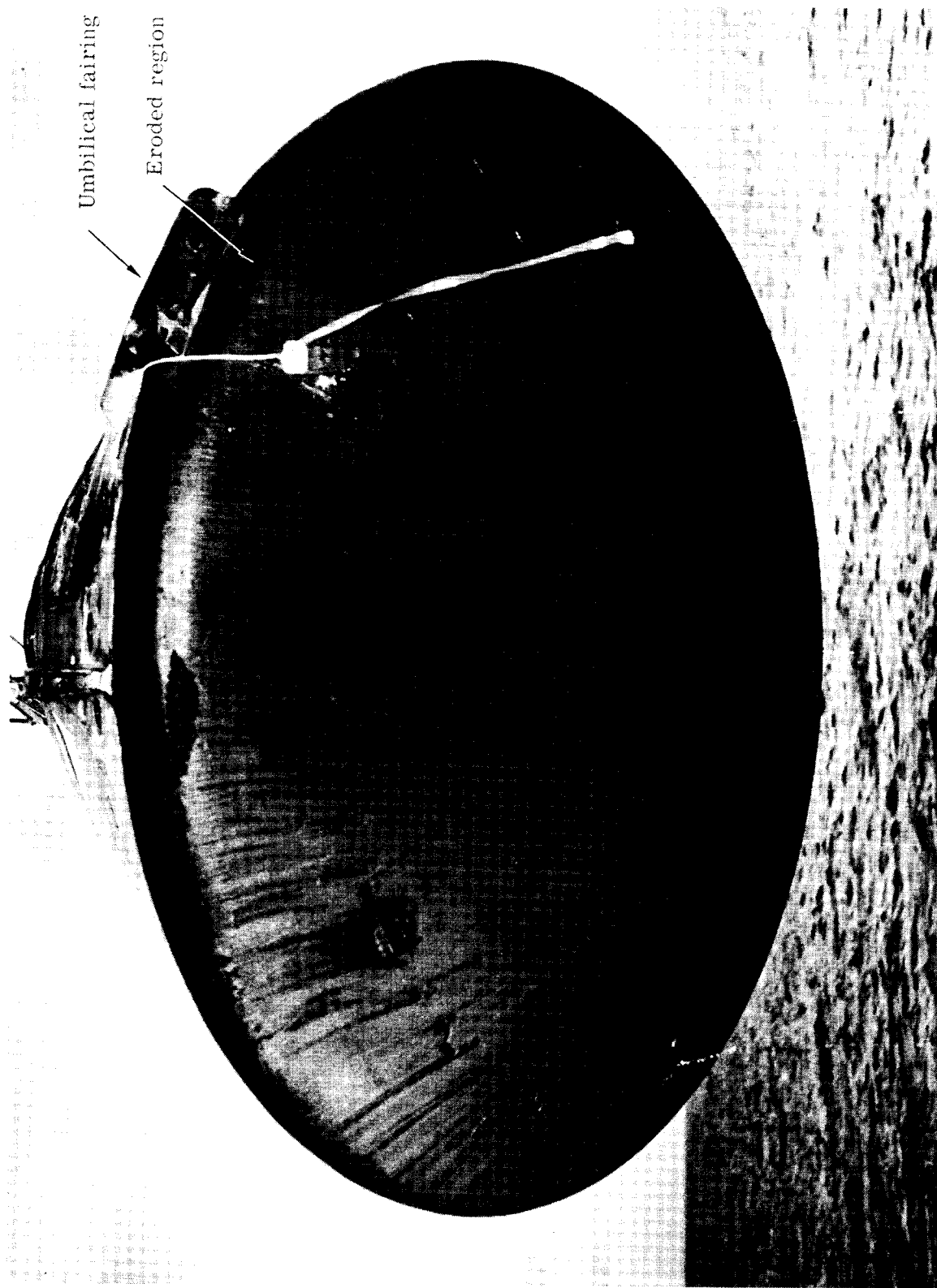
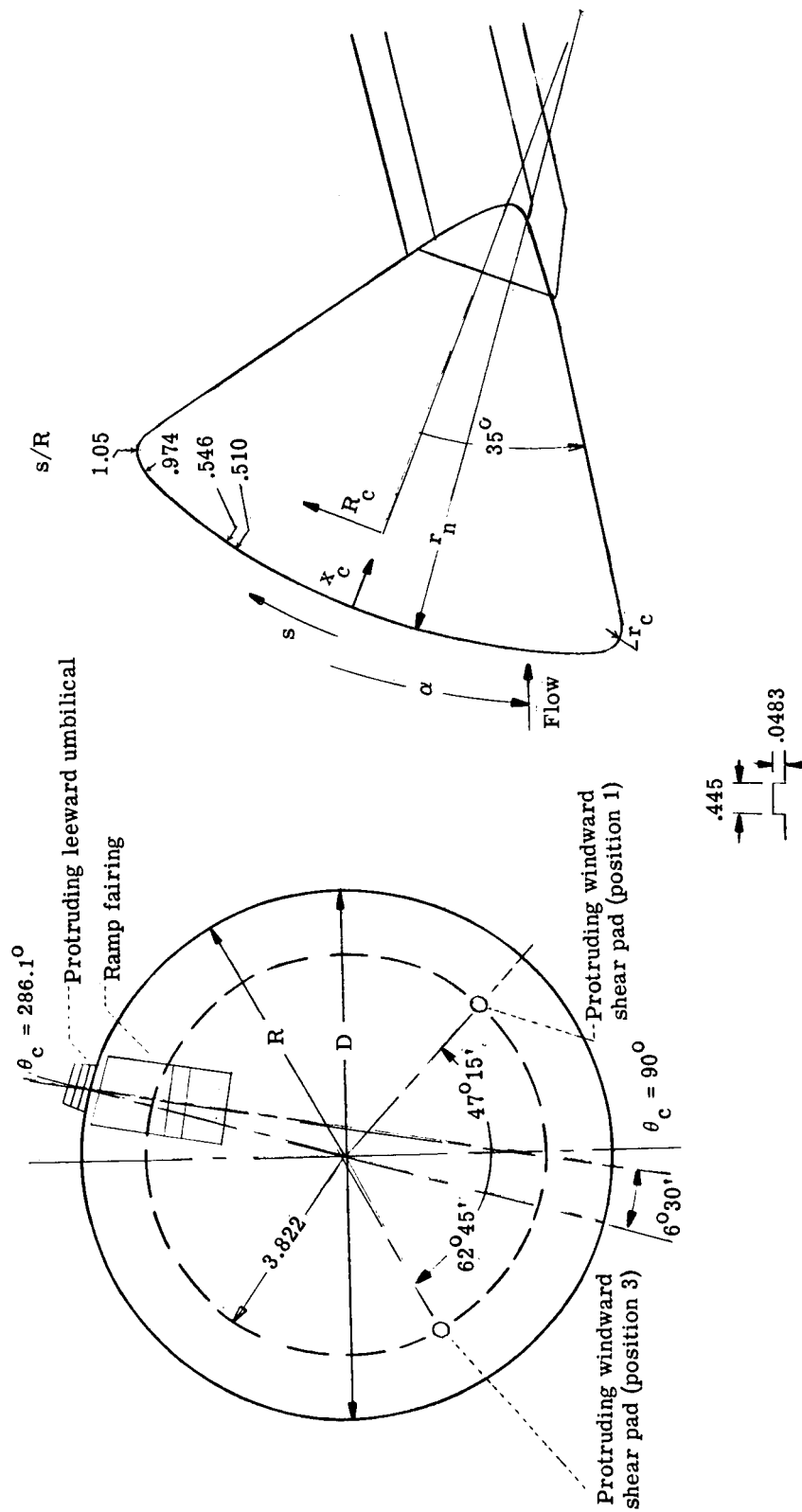


Figure 1.- Apollo heat shield immediately after qualification flight test.

S-66-22150

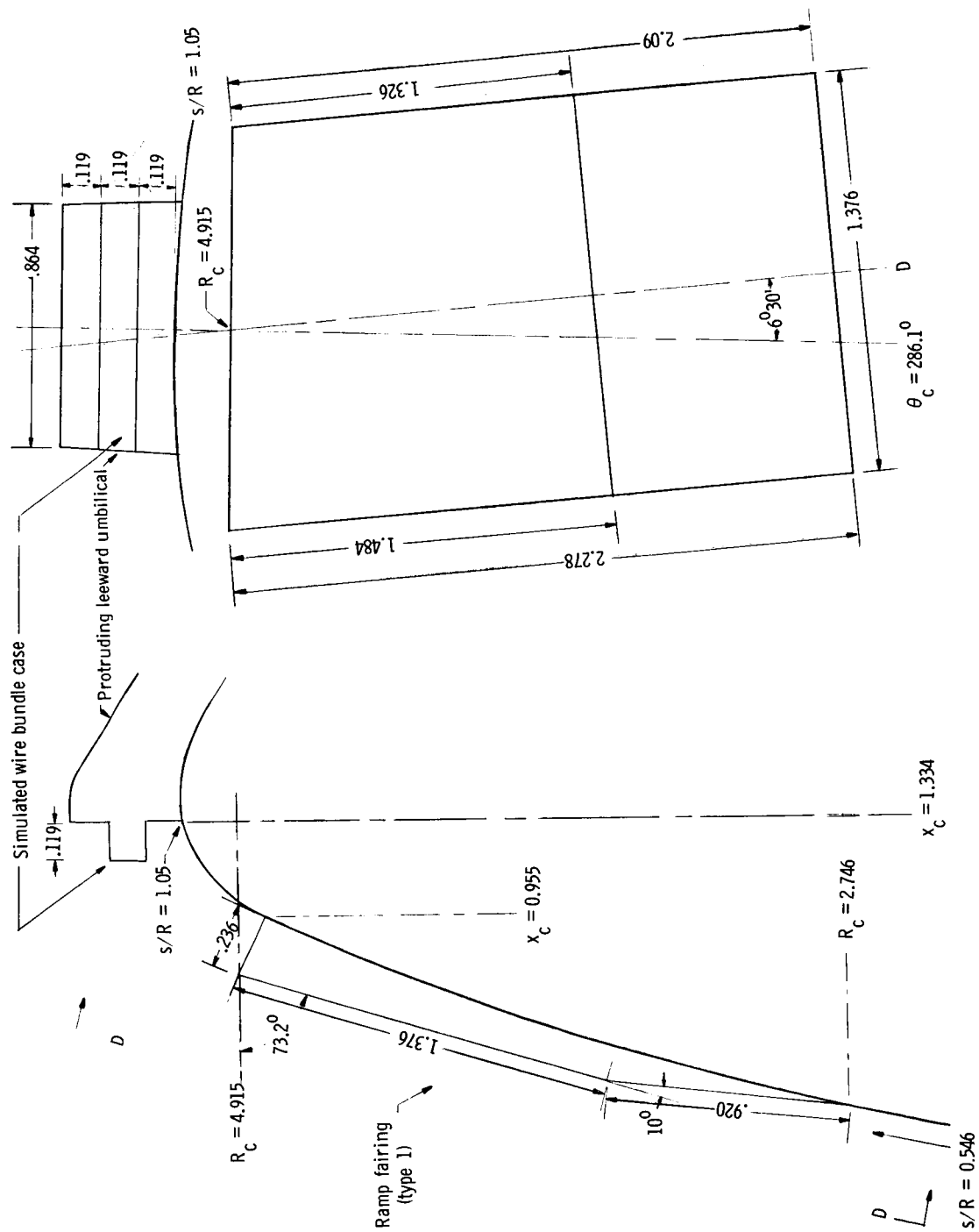


(a) View normal to face.

(b) Detail of shear pads.

(c) Side view without protuberances.

Figure 2.- Sketch of model 1. $r_n = 1.2000$; $r_c = 0.0500$; $D = 10.16$ cm. All linear dimensions are in centimeters.



(a) Profile view cut through D.

(b) Face view projected on $x_c = 1.334$ -cm plane.

Figure 4.- Detailed drawing of ramp fairing and windward face of protruding leeward umbilical on model 2. All linear dimensions are in centimeters.

Recessed pad type	Recessed pad position	Pad diam, cm	Pad depth model 3, cm	Pad depth model 4, cm
Windward shear	1	0.396	0.0396	0.0826
Windward compression	2	.635	.0330	.0660
Windward shear	3	.396	.0264	.0528
Leeward compression	4	.503	.0264	.0528
Leeward shear	5	.396	.0264	.0528
Leeward compression	6	.635	.0330	.0660

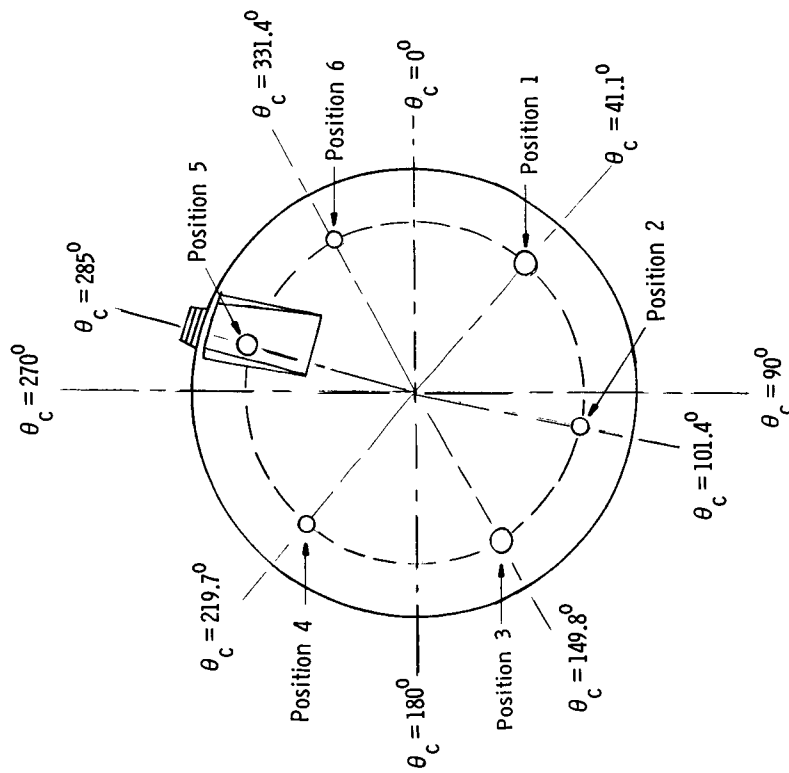


Figure 5.- Sketch of normal view of face of models 3 and 4 with table giving the respective dimensions of recessed shear and compression pads for each model.

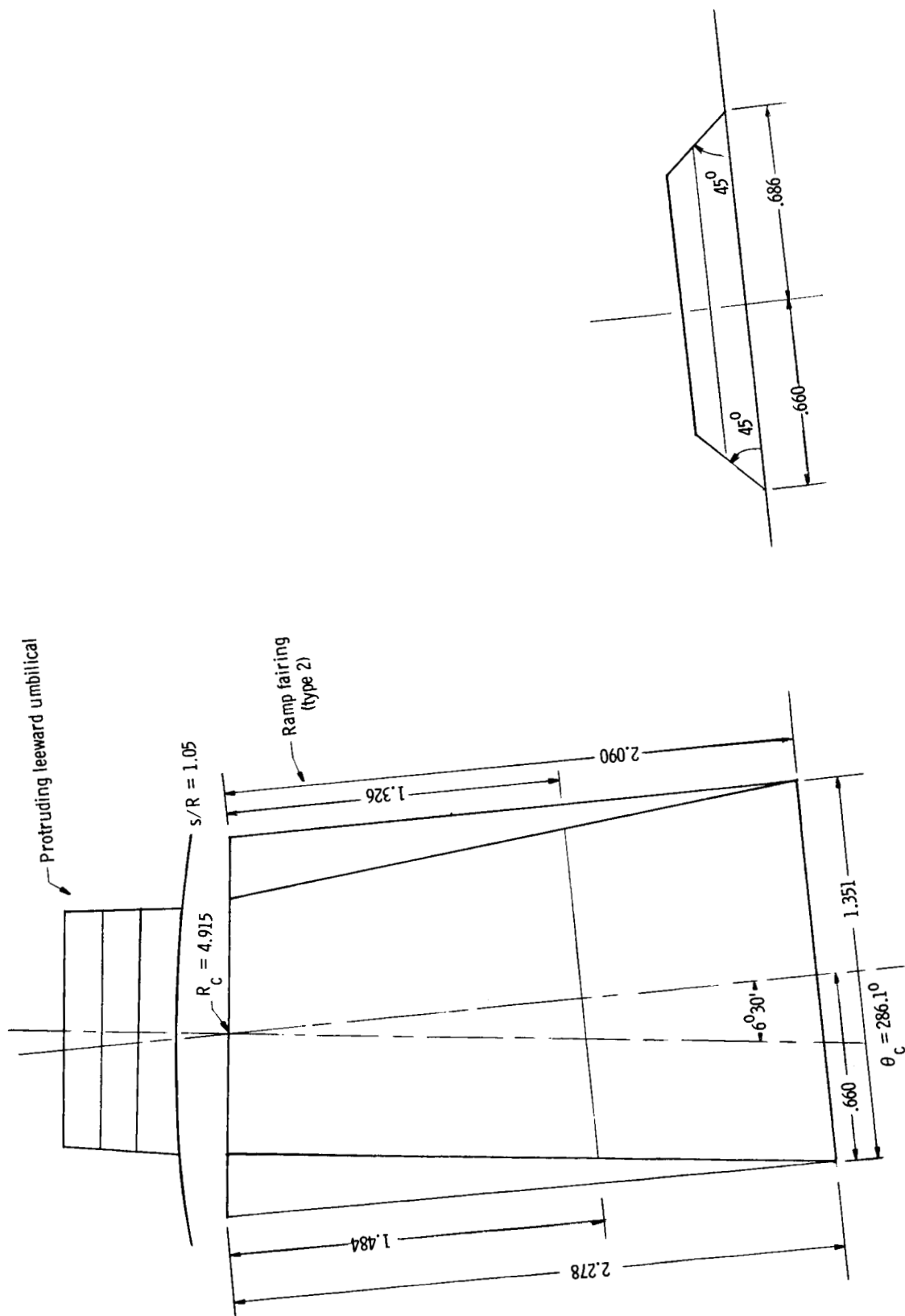
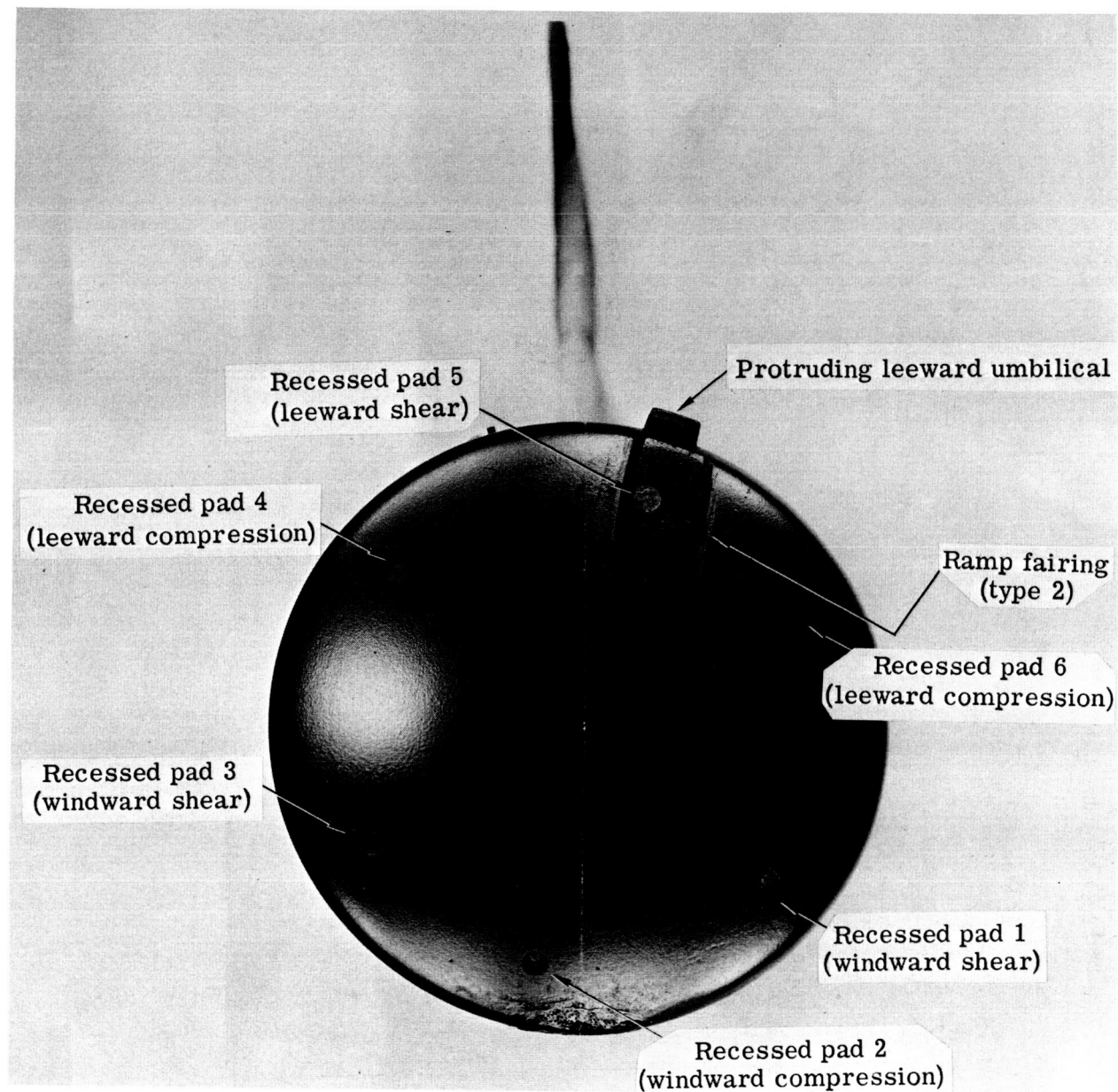


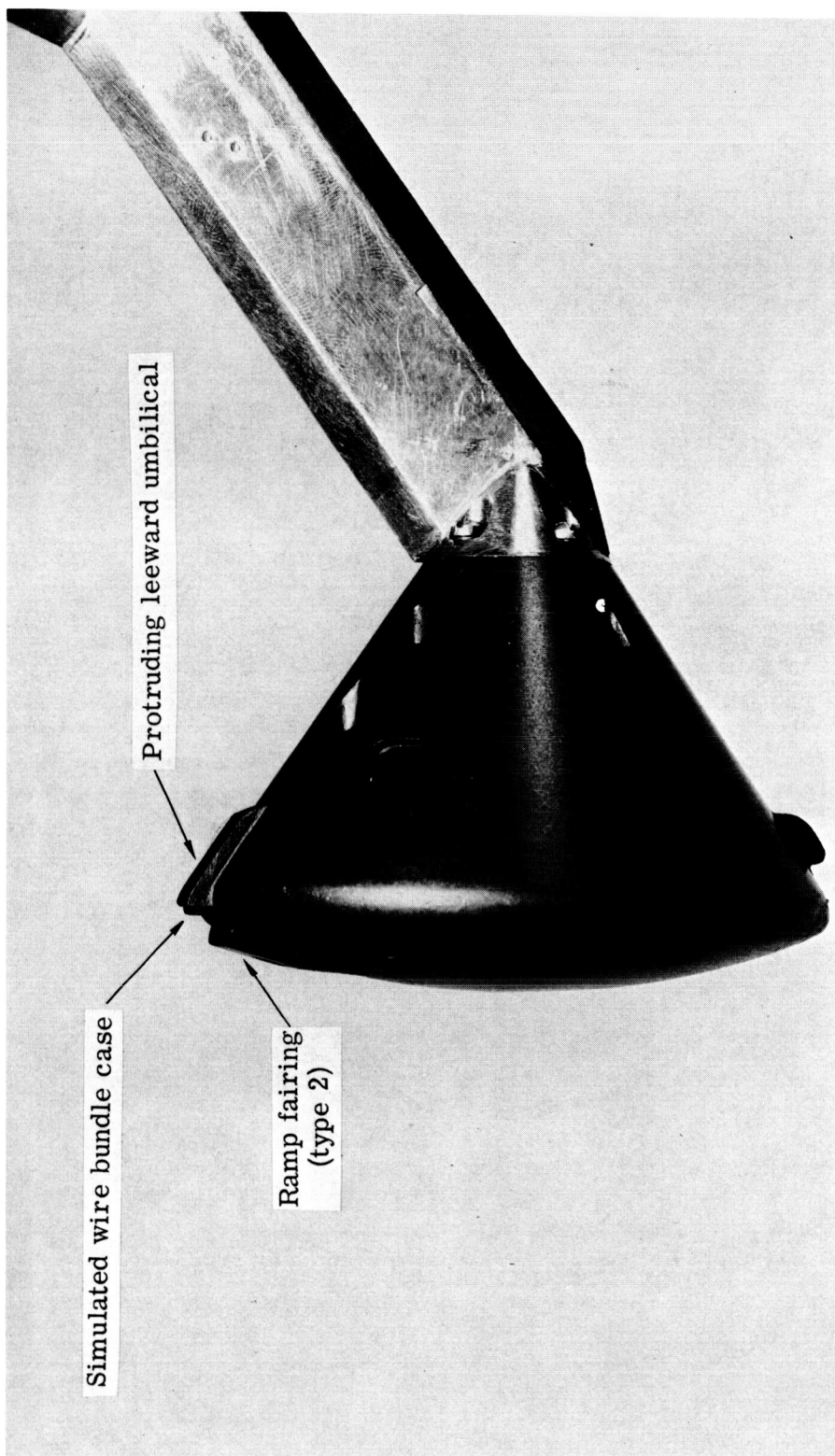
Figure 6.- Detailed drawing of beveled-edge ramp fairing for models 3 and 4. All linear dimensions are in centimeters.



(a) View normal to face.

Figure 7.- Photographs of model 4.

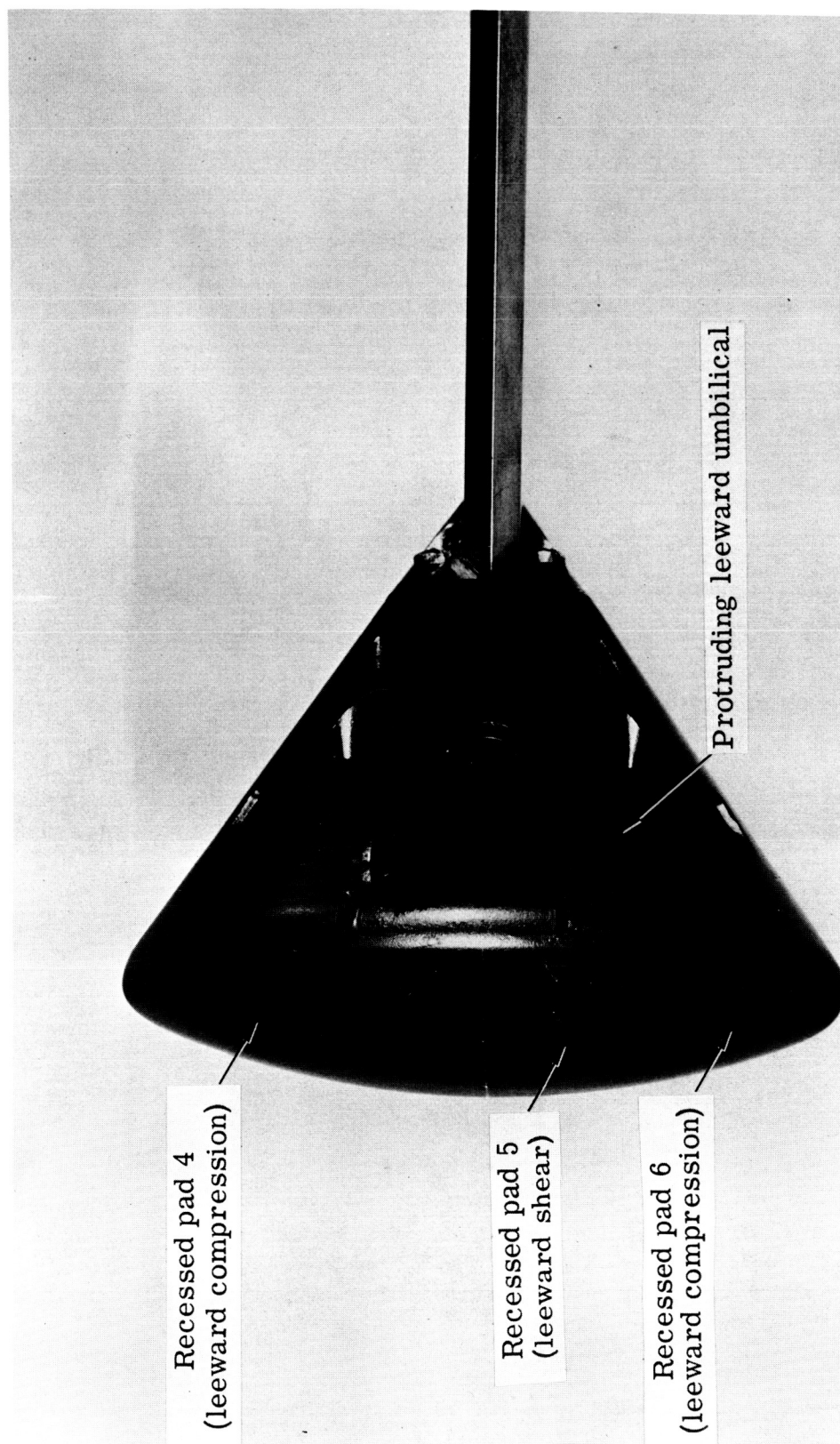
L-66-2866.1



(b) Profile view.

Figure 7.- Continued.

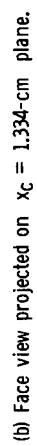
L-66-2864.1



(c) Leeward view.

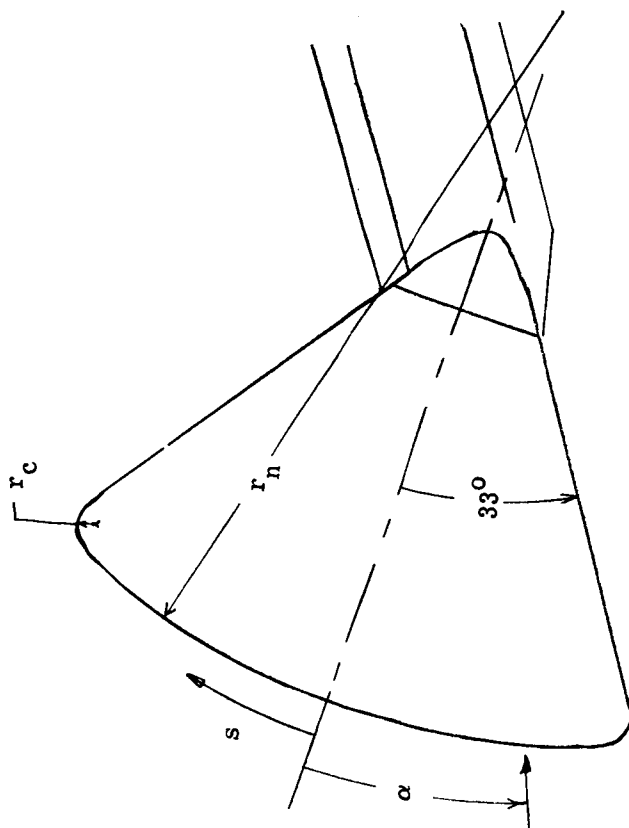
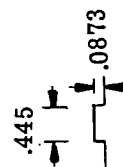
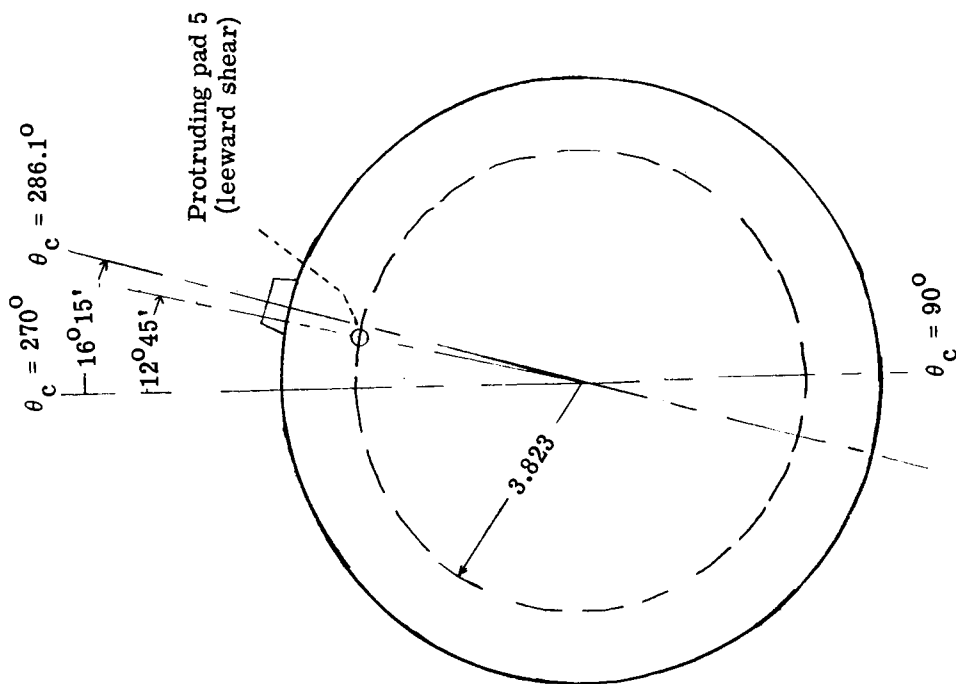
Figure 7.- Concluded.

L-66-2865.1



(a) Profile view cut through D.

Figure 8.- Detailed drawing of ramp fairing and windward face of protruding leeward umbilical on model 5. All linear dimensions are in centimeters.



(a) View normal to face. (b) Detail of shear pad 5. (c) Profile view of smooth model.
Figure 9.- Sketch of model 6. $r_n = 1.200D$; $r_c = 0.050D$; $D = 10.16$ cm. All linear dimensions are in centimeters.

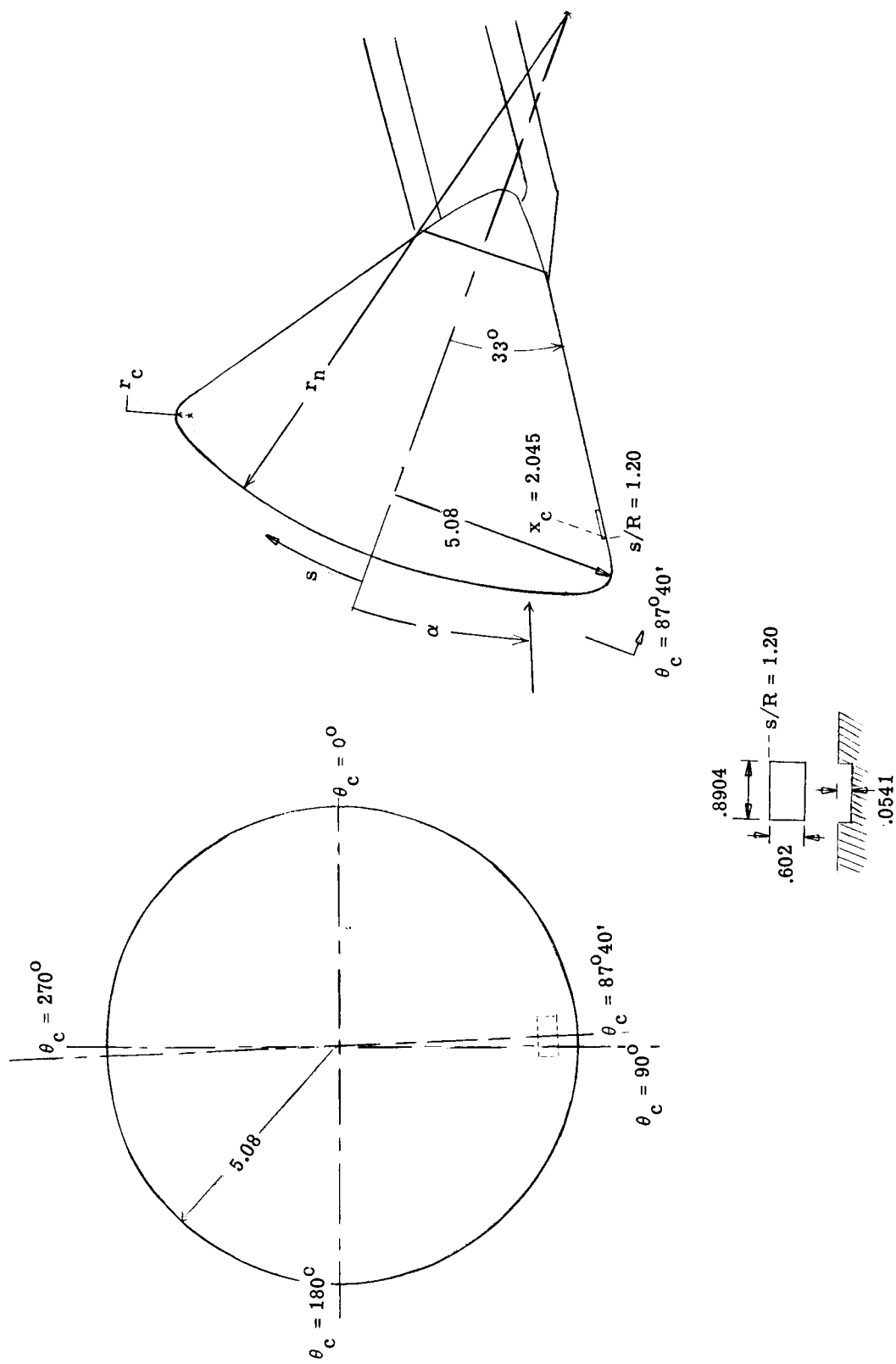


Figure 10.- Sketch of recessed windward umbilical configuration (model 7). $r_n = 1.2000$; $r_c = 0.0500$; $D = 10.16$ cm. All linear dimensions are in centimeters.

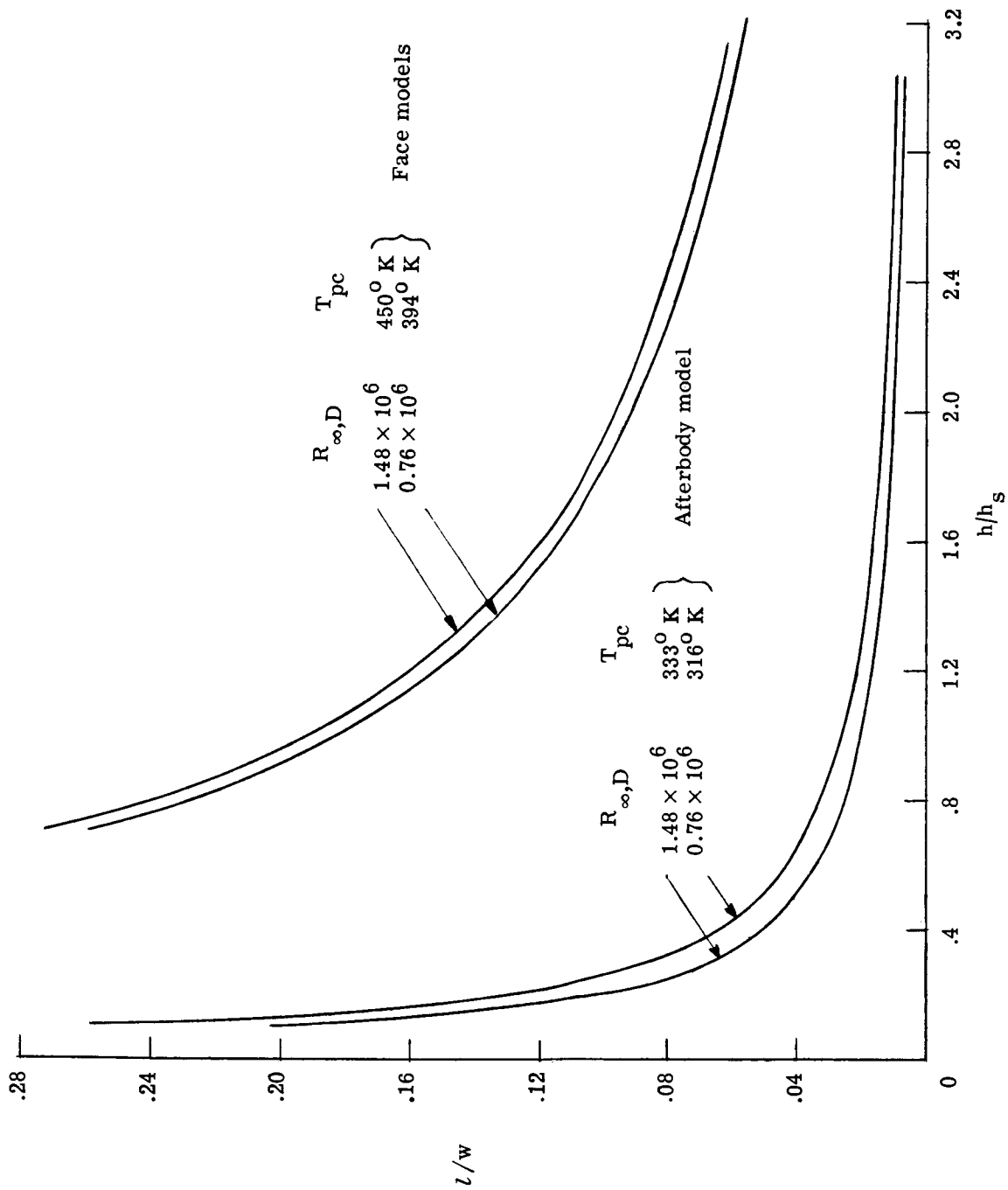


Figure 11.- Minimum distance of approach to a cavity or protuberance for which the semi-infinite slab assumption is a good approximation to the solution of the general heat-conduction equation with appropriate boundary conditions. $w = 1.376$ cm.

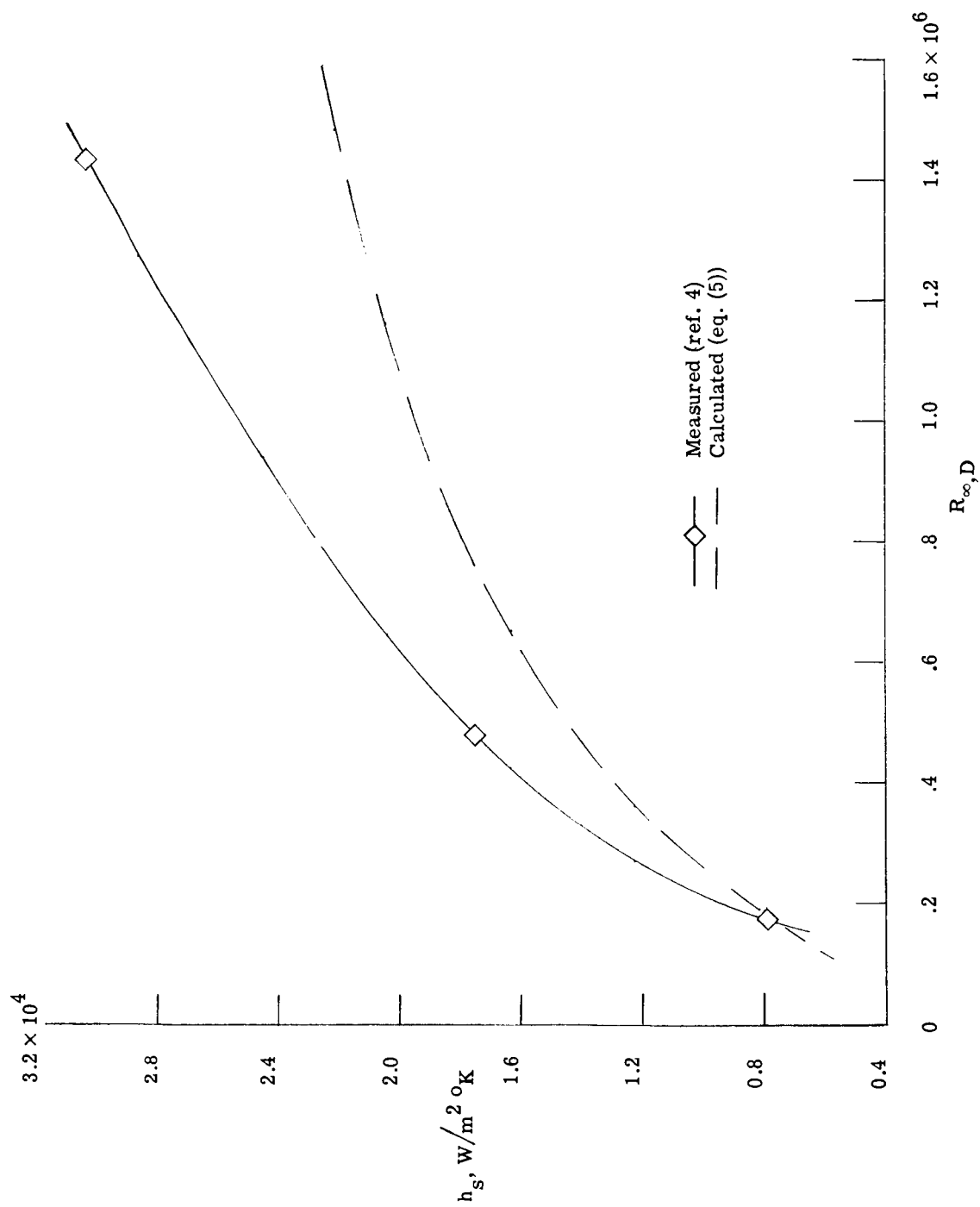


Figure 12.- Comparison of measured and calculated data for the variation of the stagnation-point heat-transfer coefficients at $\alpha = 0^\circ$ with free-stream Reynolds number based on the model diameter.

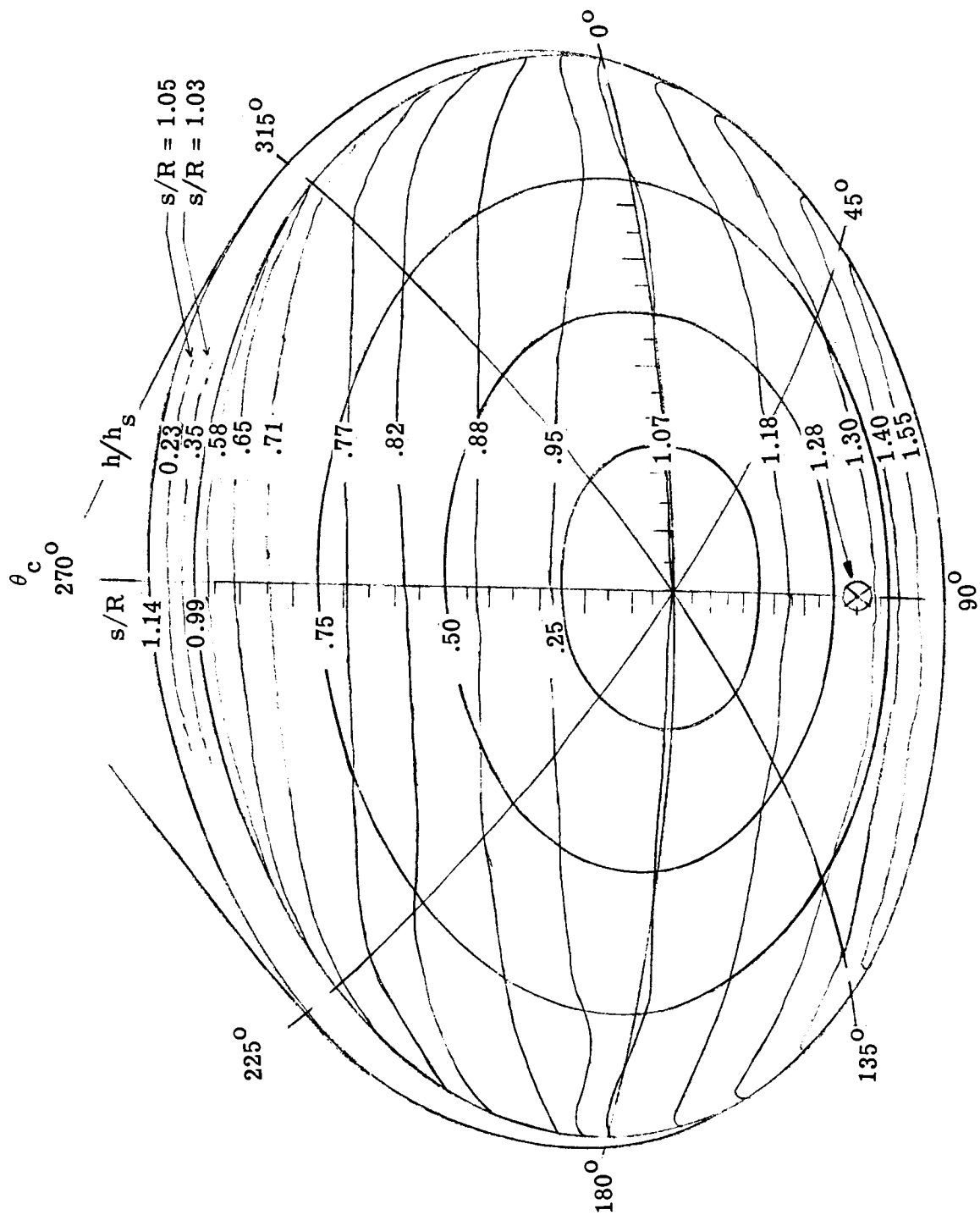
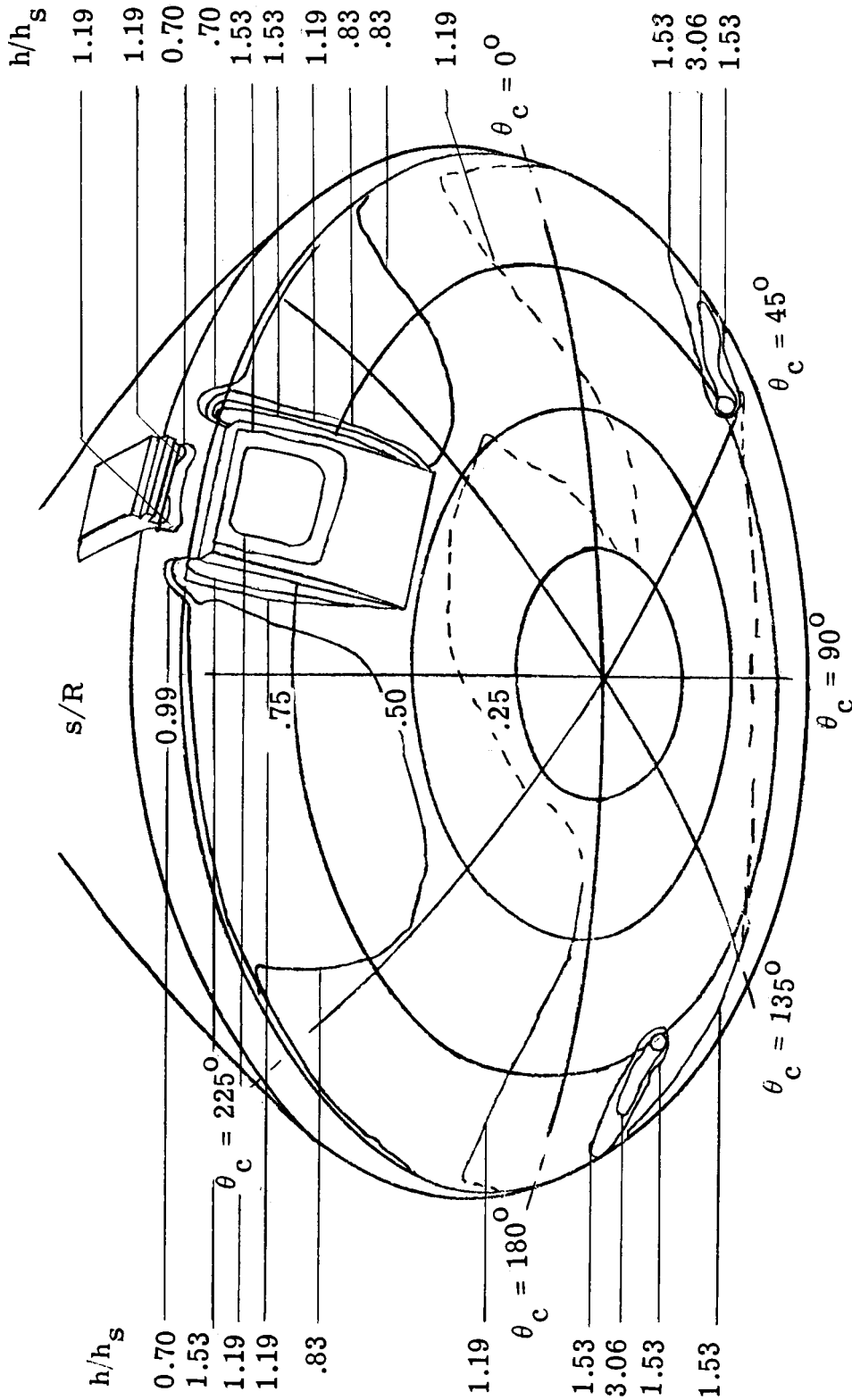
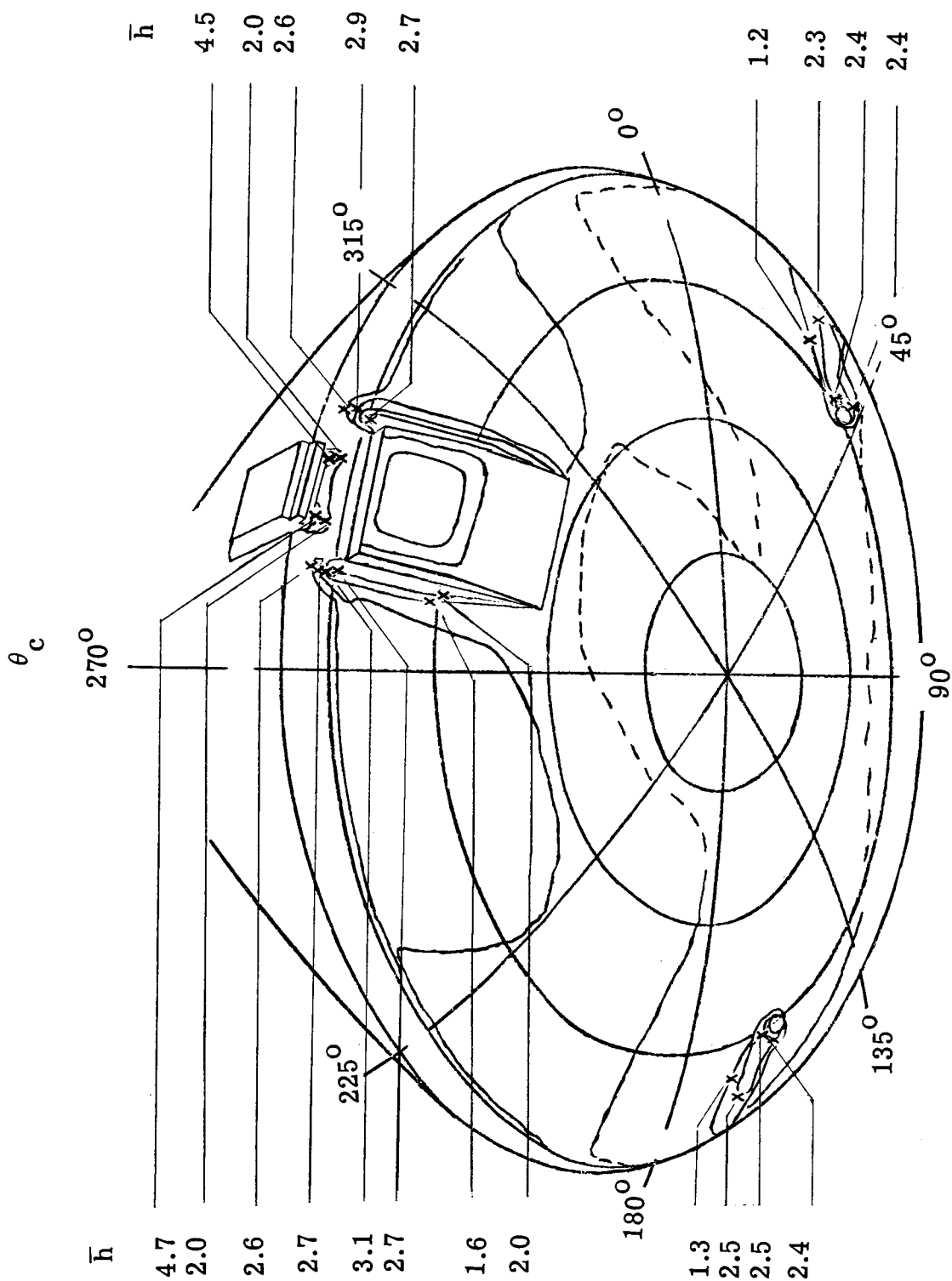


Figure 13.- Heat-transfer-coefficient-ratio contours on face of smooth body (model 8). $R_{\infty,D} = 0.76 \times 10^6$; $\alpha = 22^\circ$; $h_s = 1.755 \times 10^2 \text{ W/m}^2\text{-}^\circ\text{K}$.



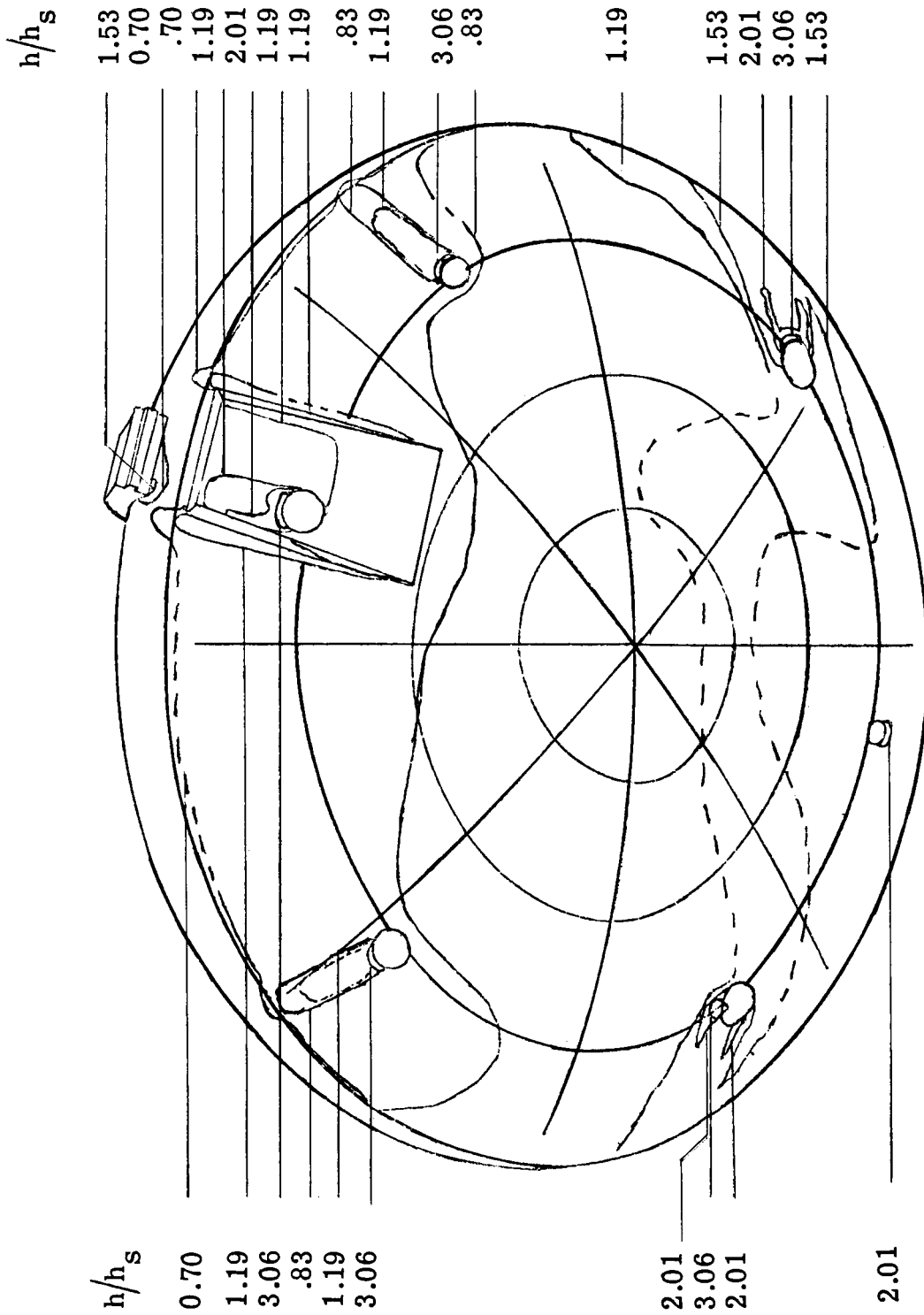
(a) Heat-transfer-coefficient contours.

Figure 14.- Interference heating on face of model 2. $R_{\infty} D = 0.76 \times 10^6$; $\alpha = 22^\circ$; $h_s = 1.755 \times 10^2 \text{ W/m}^2\text{-}^\circ\text{K}$.



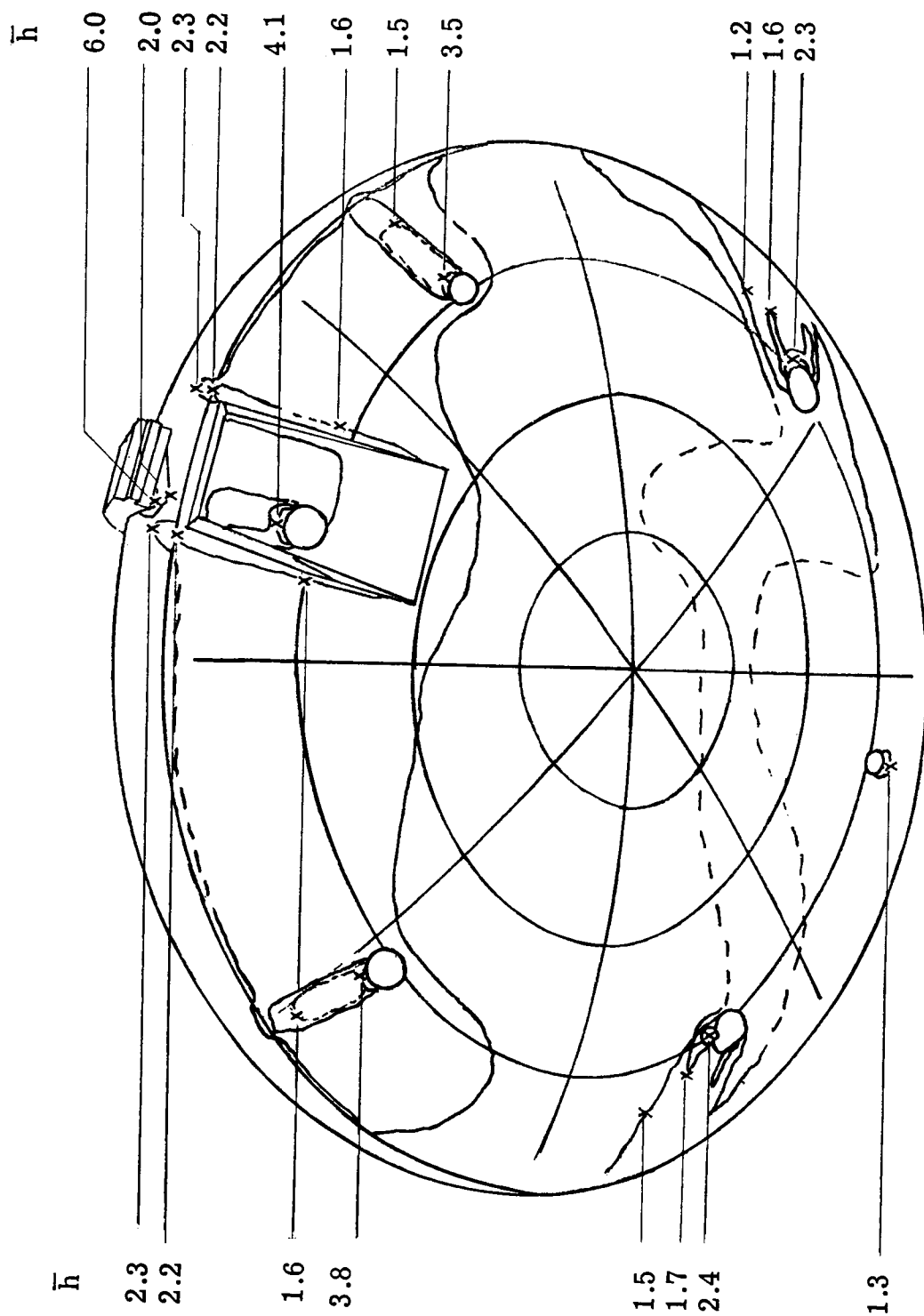
(b) Interference heating factors.

Figure 14.- Concluded.



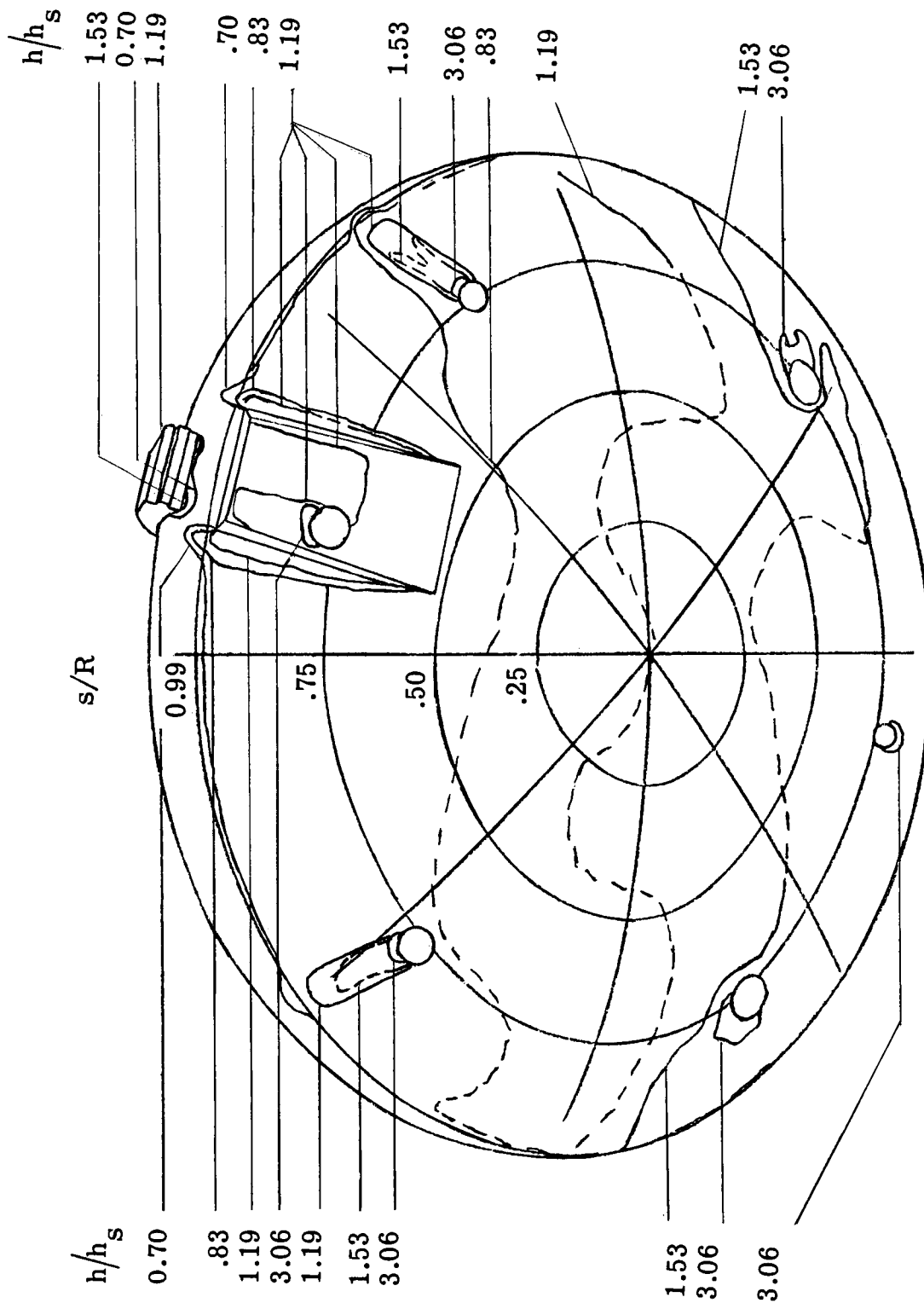
(a) Heat-transfer-coefficient contours.

Figure 15.- Interference heating on face of model 3. $R_{\infty}D = 0.76 \times 10^6$; $\alpha = 22^\circ$; $h_s = 1.774 \times 10^2 \text{ W/m}^2\text{-}^\circ\text{K}$.



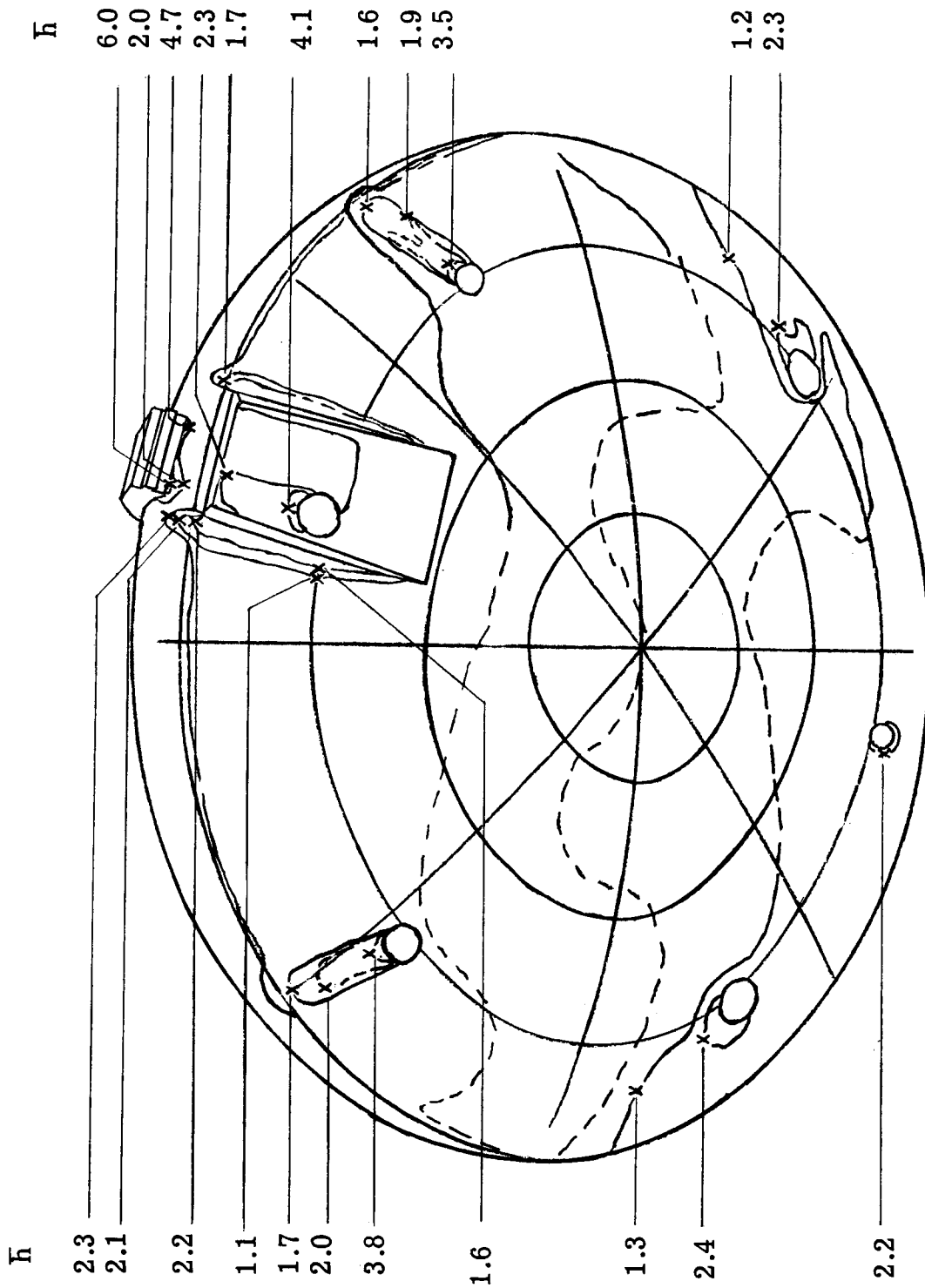
(b) Interference heating factors.

Figure 15.- Concluded.



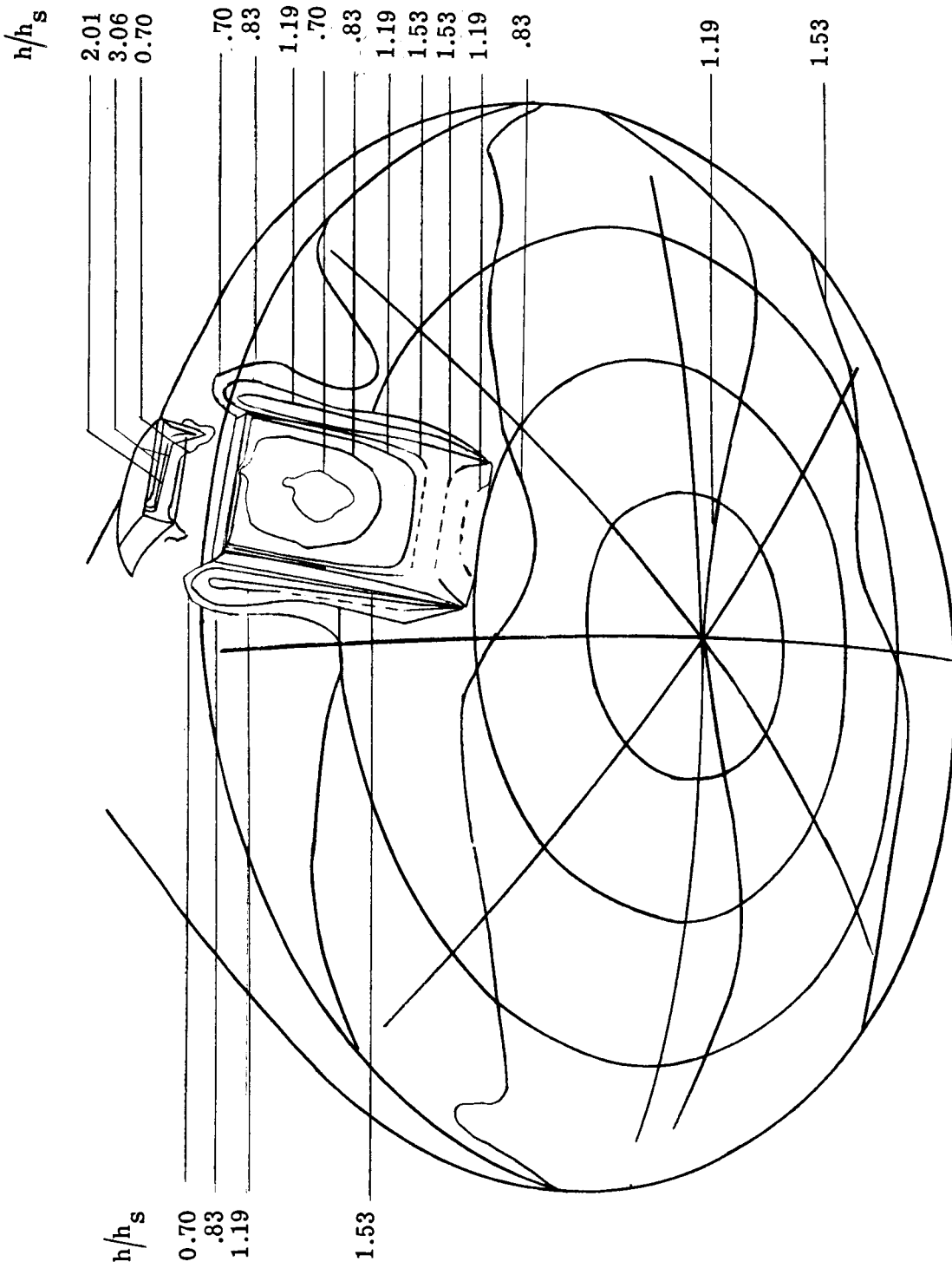
(a) Heat-transfer-coefficient contours.

Figure 16.- Interference heating on face of model 4. $R_{\infty,D} = 0.76 \times 10^6$; $\alpha = 22^\circ$; $h_s = 1.749 \times 10^2 \text{ W/m}^2\text{-}^\circ\text{K}$.



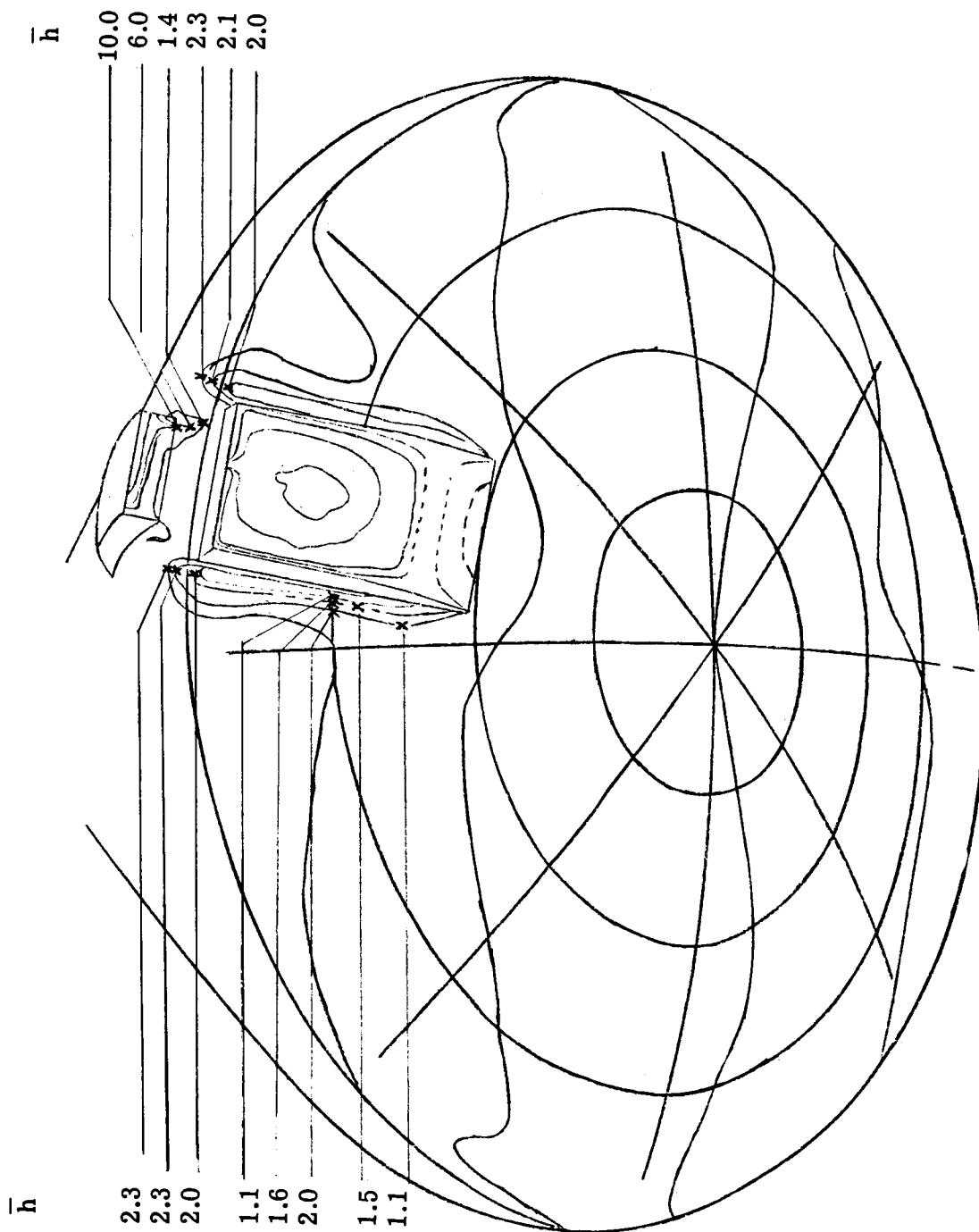
(b) Interference heating factors.

Figure 16.- Concluded.



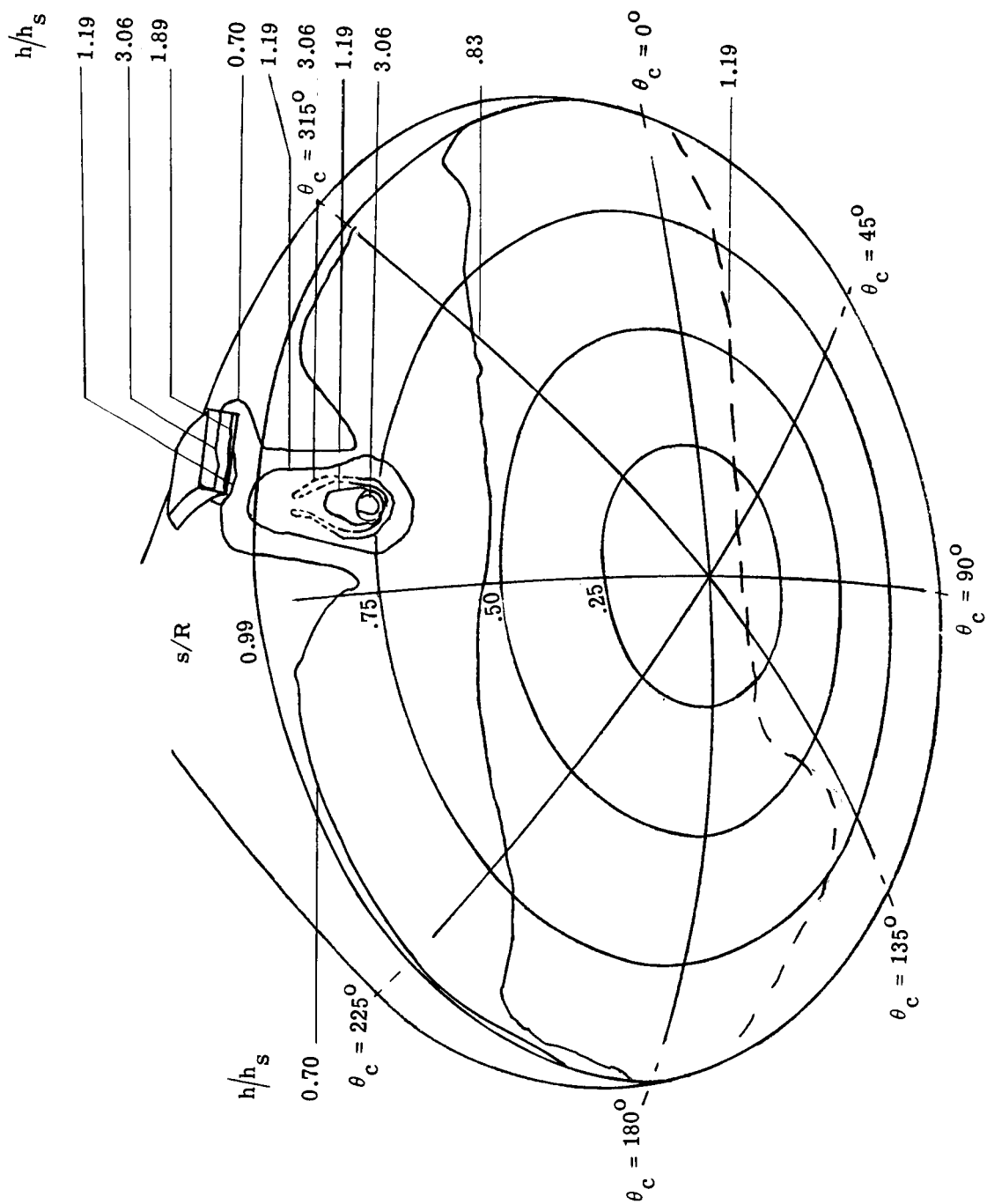
(a) Heat-transfer-coefficient contours.

Figure 17.- Interference heating on face of model 5. $R_{\infty,D} = 0.76 \times 10^6$; $\alpha = 22^\circ$; $h_s = 1.765 \times 10^2 \text{ W/m}^2\text{-}^\circ\text{K}$.



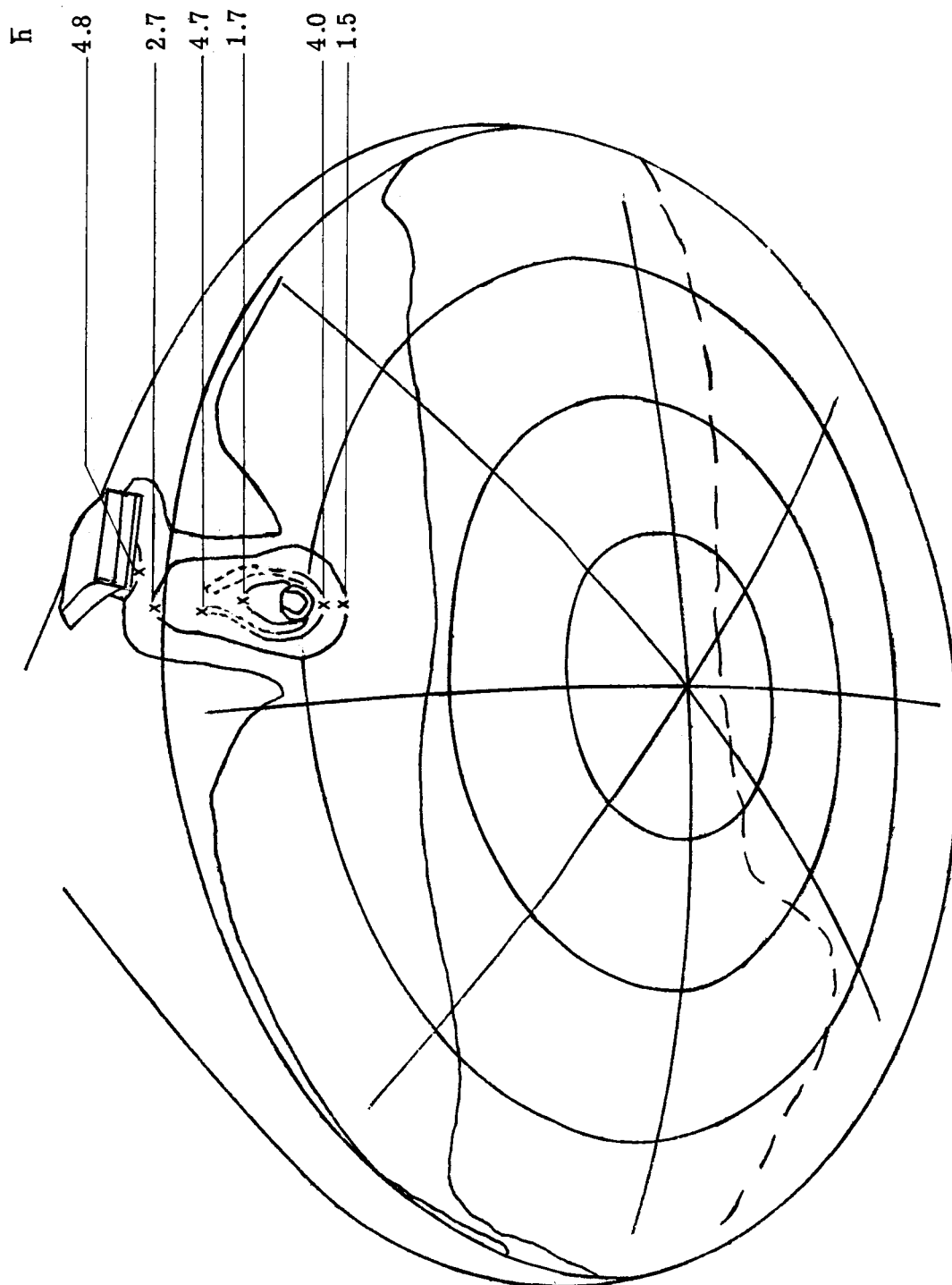
(b) Interference heating factors.

Figure 17.- Concluded.



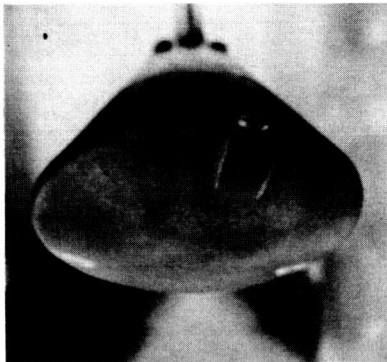
(a) Heat-transfer-coefficient contours.

Figure 18.- Interference heating on face of model 6. $R_{\infty,D} = 0.76 \times 10^6$, $\alpha = 22^\circ$, $h_s = 1.765 \times 10^2 \text{ W/m}^2\text{-}^\circ\text{K}$.

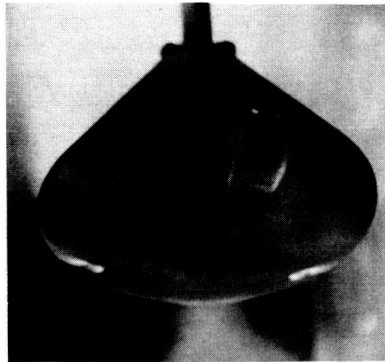


(b) Interference heating factors.

Figure 18.- Concluded.

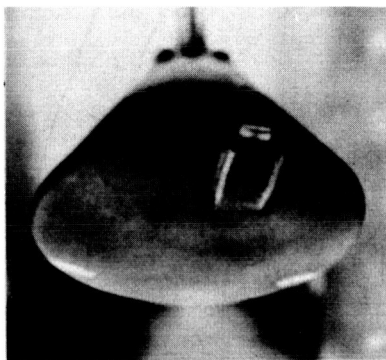


$\alpha = 18^\circ$

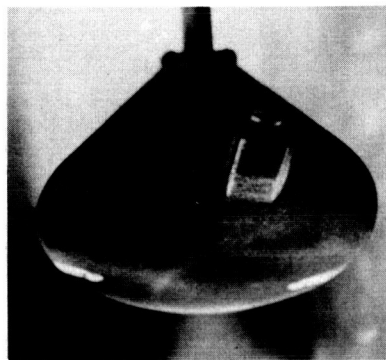


$\alpha = 22^\circ$

(a) $h/h_s = 3.06$.

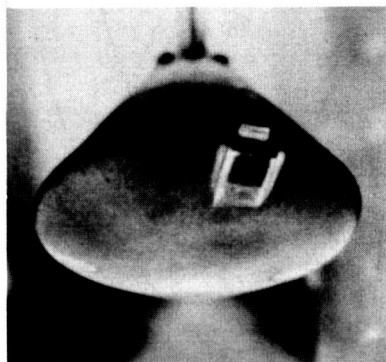


$\alpha = 18^\circ$

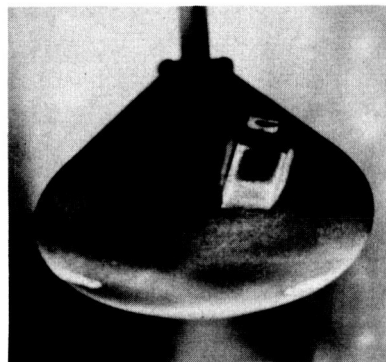


$\alpha = 22^\circ$

(b) $h/h_s = 2.01$.



$\alpha = 18^\circ$

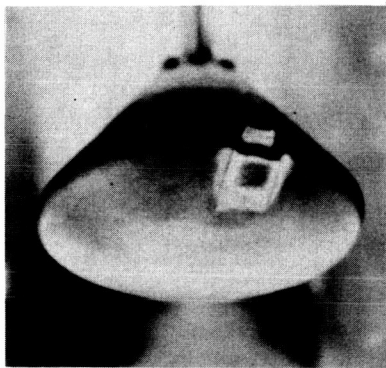


$\alpha = 22^\circ$

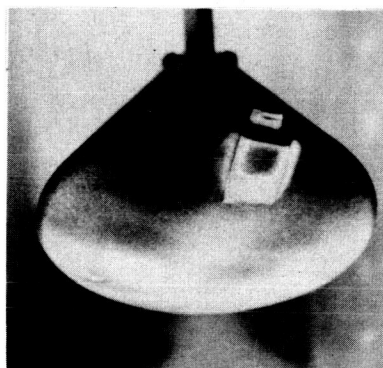
(c) $h/h_s = 1.53$.

Figure 19.- Phase-change patterns for model 2. $R_{\infty,D} = 0.76 \times 10^6$.

L-68-5613

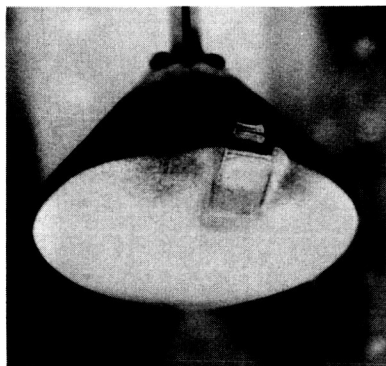


$\alpha = 18^{\circ}$

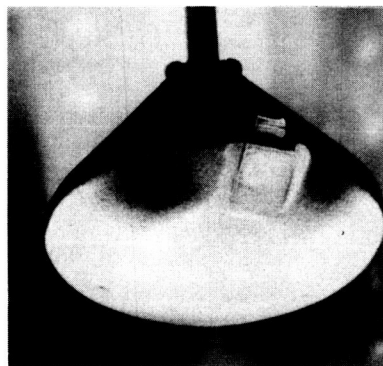


$\alpha = 22^{\circ}$

(d) $h/h_S = 1.19$.

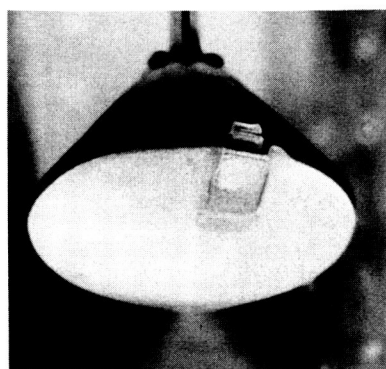


$\alpha = 18^{\circ}$

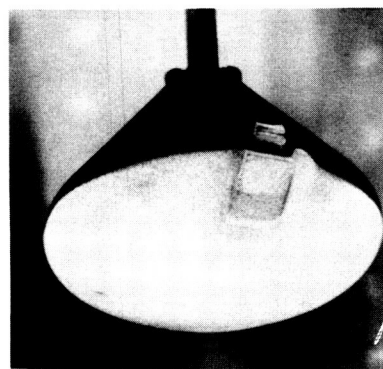


$\alpha = 22^{\circ}$

(e) $h/h_S = 0.83$.



$\alpha = 18^{\circ}$

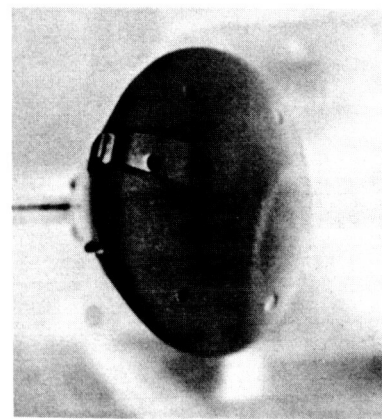


$\alpha = 22^{\circ}$

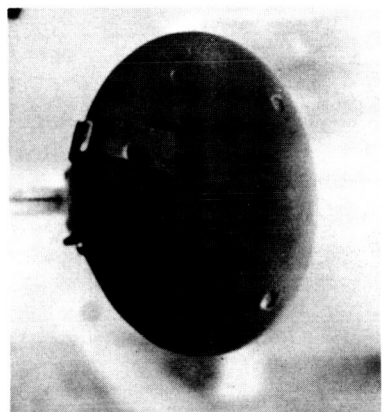
(f) $h/h_S = 0.70$.

Figure 19.- Concluded.

L-68-5614

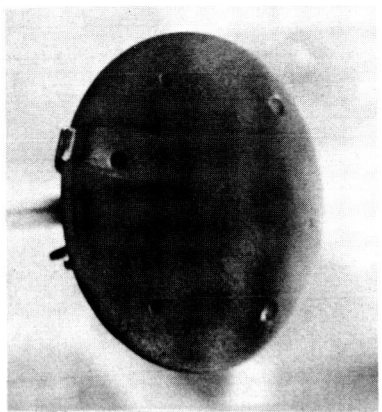


$\alpha = 18^\circ$

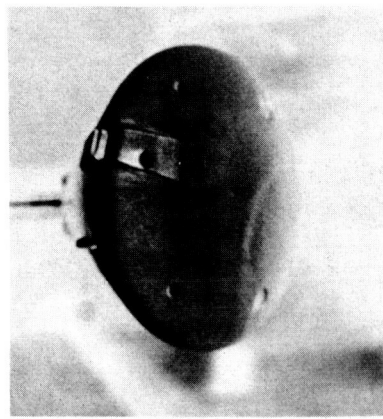


$\alpha = 22^\circ$

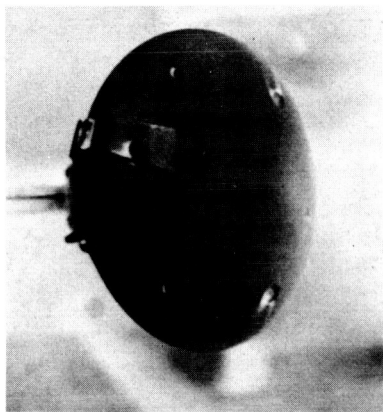
(a) $h/h_s = 3.06$.



$\alpha = 26^\circ$

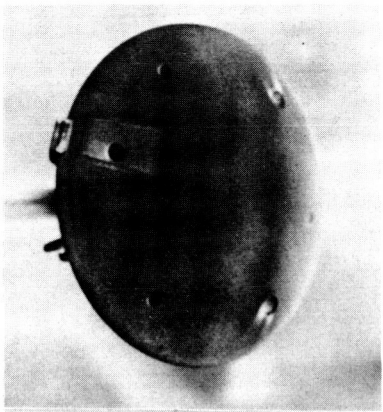


$\alpha = 18^\circ$



$\alpha = 22^\circ$

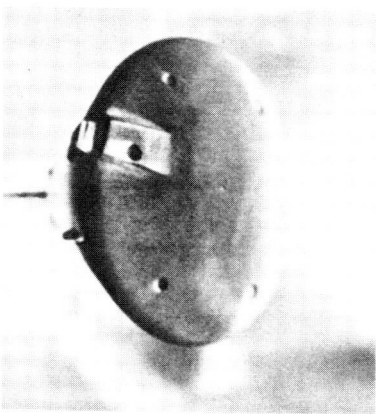
(b) $h/h_s = 2.01$.



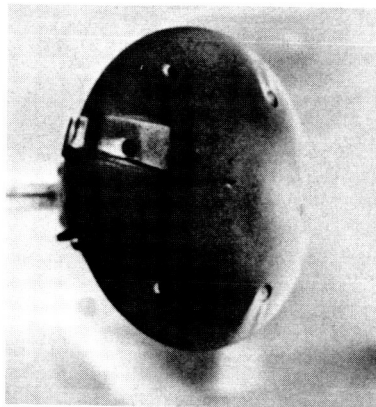
$\alpha = 26^\circ$

Figure 20.- Phase-change patterns for model 3. $R_{\infty,D} = 0.76 \times 10^6$.

L-68-5615

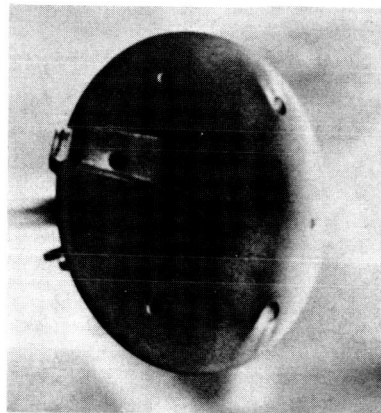


$\alpha = 18^\circ$

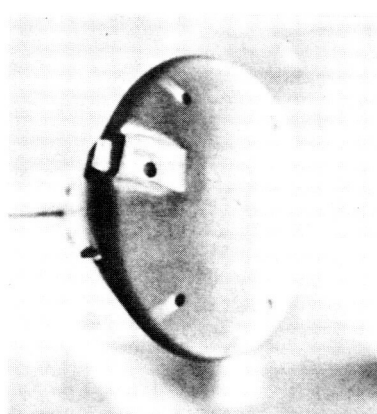


$\alpha = 22^\circ$

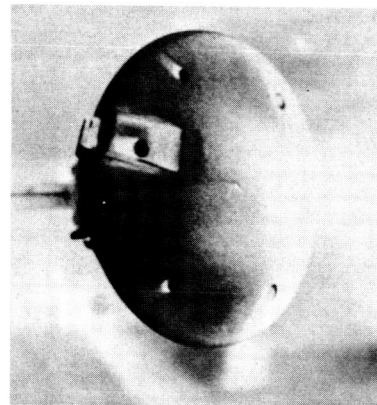
(c) $h/h_s = 1.53$.



$\alpha = 26^\circ$

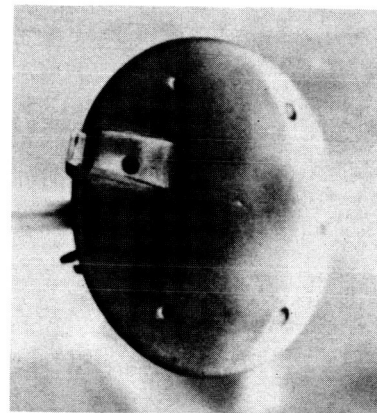


$\alpha = 18^\circ$



$\alpha = 22^\circ$

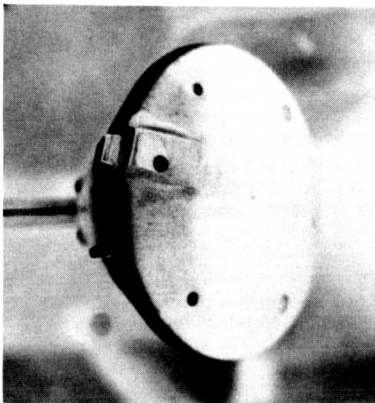
(d) $h/h_s = 1.19$.



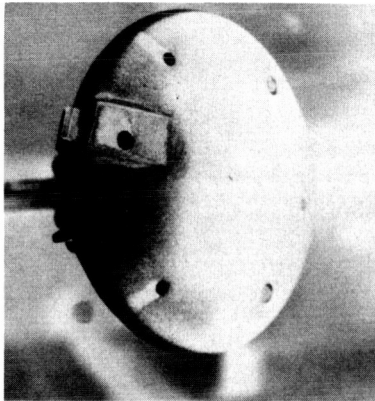
$\alpha = 26^\circ$

Figure 20.- Continued.

L-68-5616

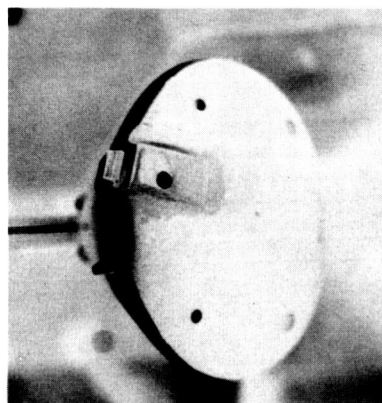


$\alpha = 18^\circ$

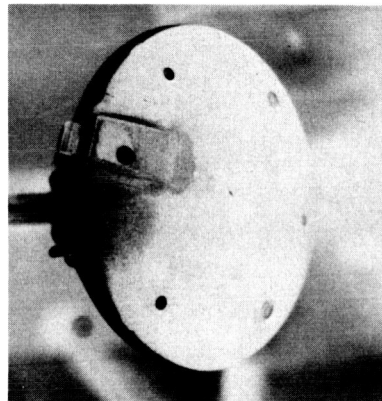


$\alpha = 22^\circ$

(e) $h/h_s = 0.83$.



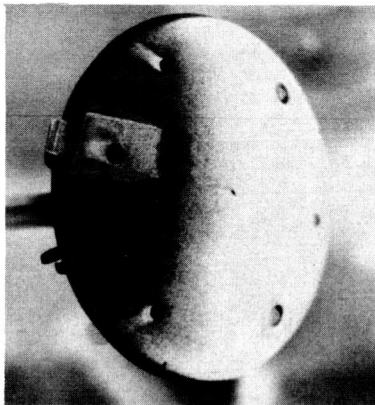
$\alpha = 18^\circ$



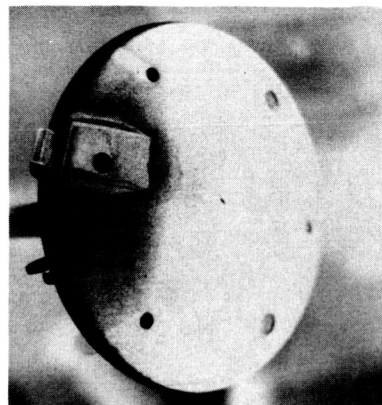
$\alpha = 22^\circ$

(f) $h/h_s = 0.70$.

Figure 20.- Concluded.

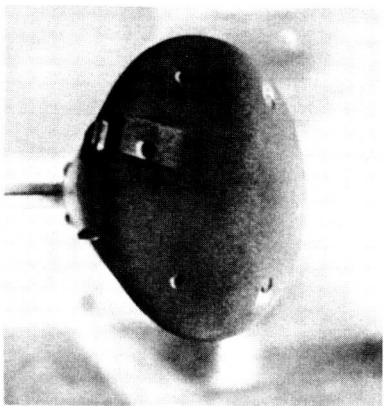


$\alpha = 26^\circ$

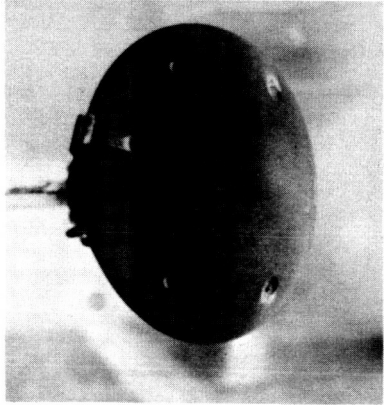


$\alpha = 26^\circ$

L-68-5617

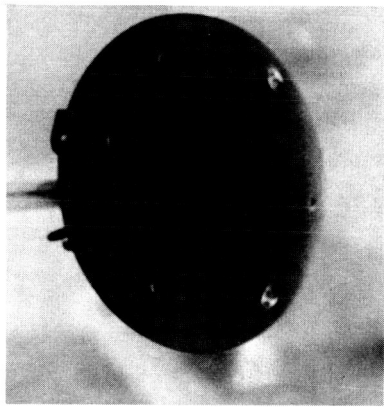


$\alpha = 18^\circ$

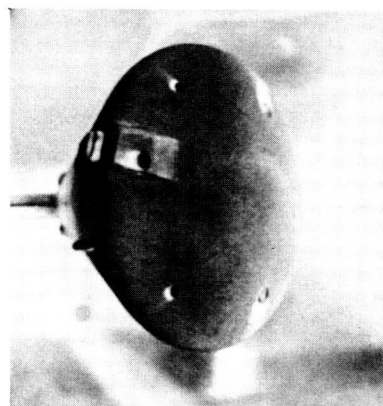


$\alpha = 22^\circ$

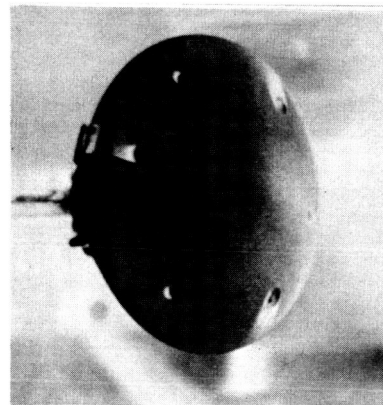
(a) $h/h_s = 3.06$.



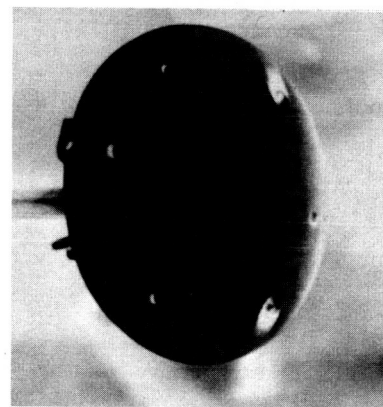
$\alpha = 26^\circ$



$\alpha = 18^\circ$



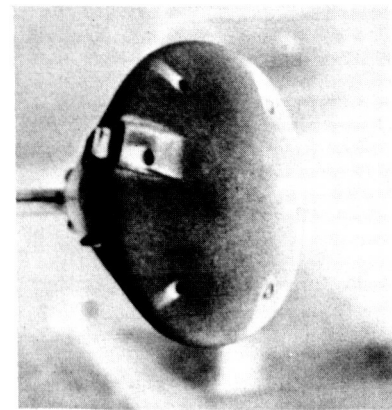
$\alpha = 22^\circ$



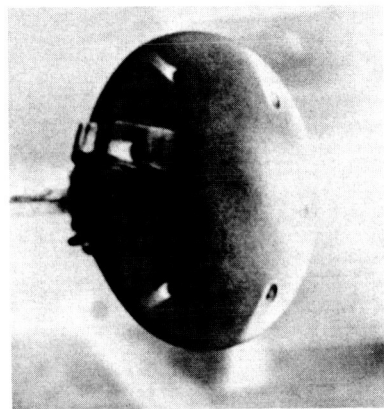
$\alpha = 26^\circ$

(b) $h/h_s = 2.01$.
Figure 21.- Phase-change patterns for model 4. $R_{\infty,p} = 0.76 \times 10^6$.

L-68-5618

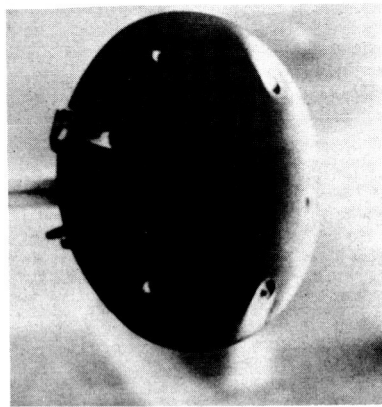


$\alpha = 18^\circ$

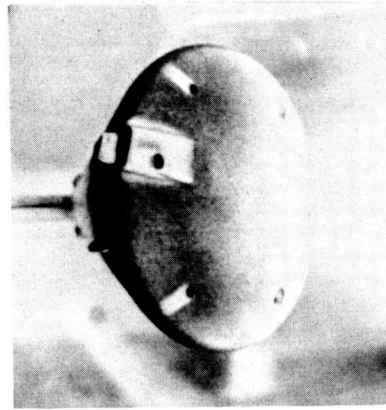


$\alpha = 22^\circ$

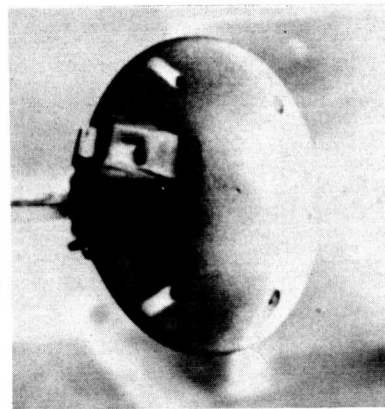
(c) $h/h_s = 1.53$.



$\alpha = 26^\circ$

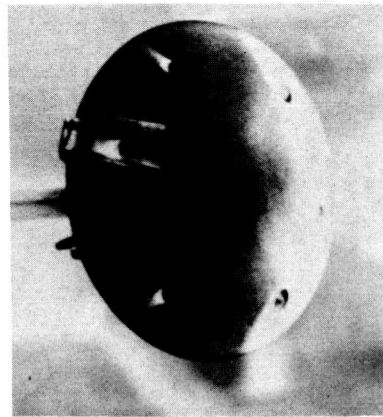


$\alpha = 18^\circ$



$\alpha = 22^\circ$

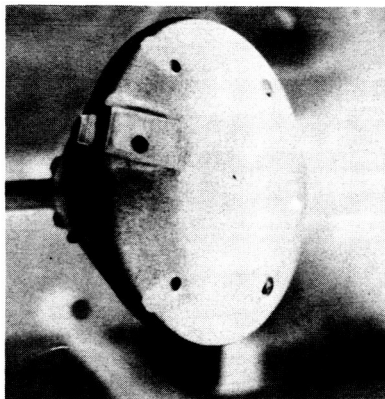
(d) $h/h_s = 1.19$.



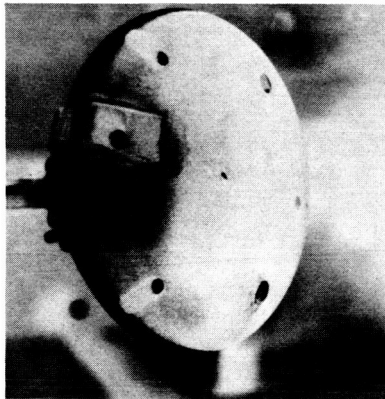
$\alpha = 26^\circ$

Figure 21.- Continued.

L-68-5619

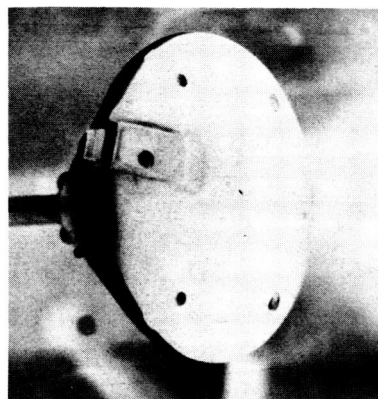


$\alpha = 18^\circ$

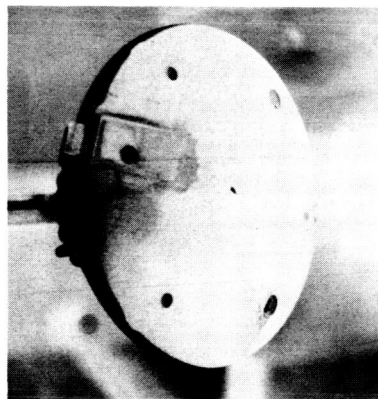


$\alpha = 22^\circ$

(e) $h/h_s = 0.83$.



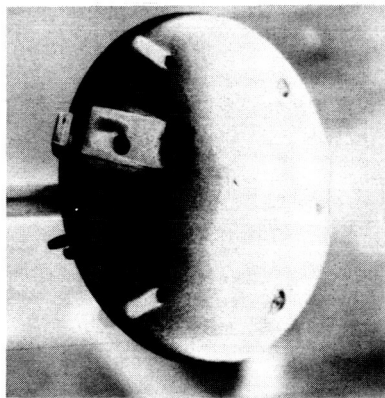
$\alpha = 18^\circ$



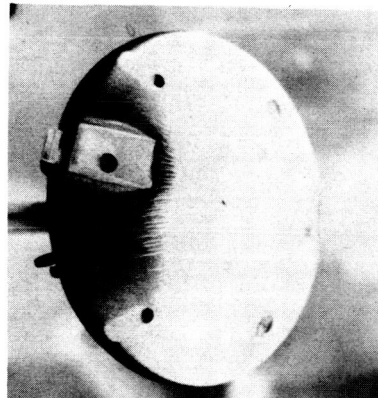
$\alpha = 22^\circ$

(f) $h/h_s = 0.70$.

Figure 21.- Concluded.

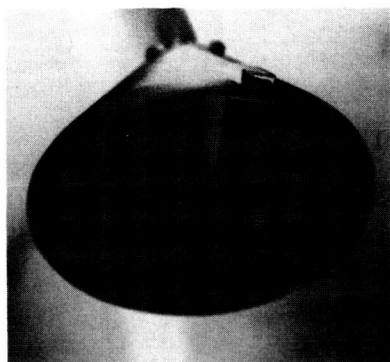


$\alpha = 26^\circ$

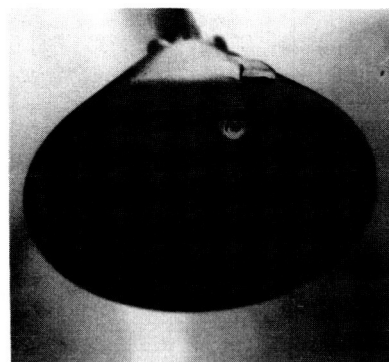


$\alpha = 26^\circ$

L-68-5620

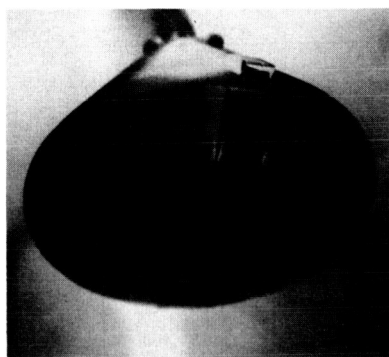


Model 5

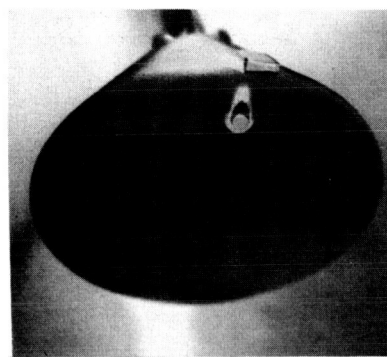


Model 6

(a) $h/h_s = 3.06$.

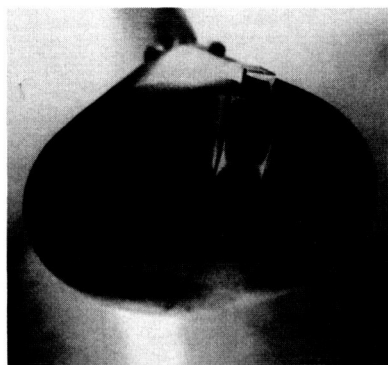


Model 5

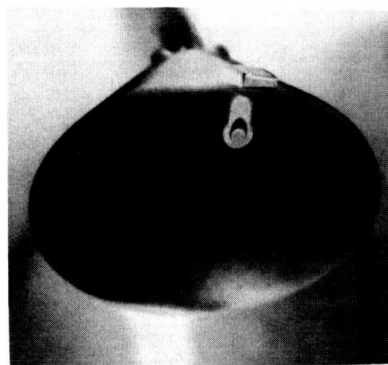


Model 6

(b) $h/h_s = 2.01$.



Model 5

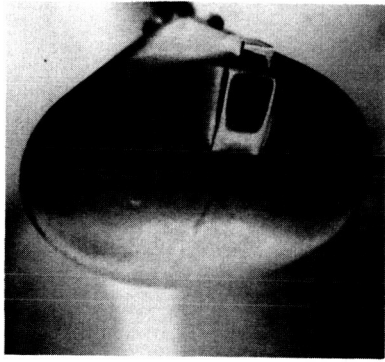


Model 6

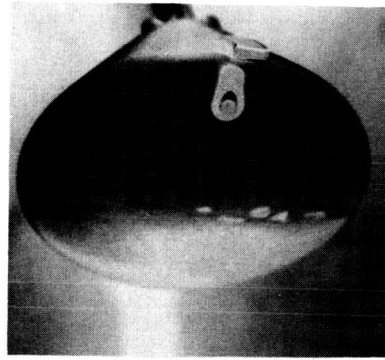
(c) $h/h_s = 1.53$.

Figure 22.- Phase-change patterns for models 5 and 6. $\alpha = 22^\circ$; $R_{\infty,D} = 0.76 \times 10^6$.

L-68-5621

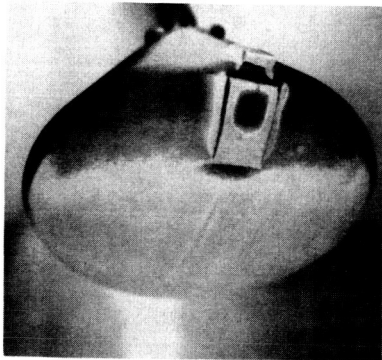


Model 5

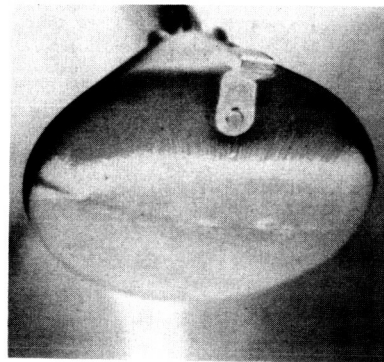


Model 6

(d) $h/h_s = 1.19$.

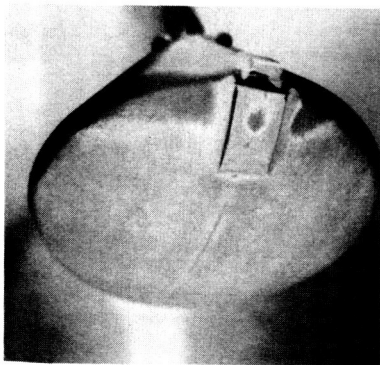


Model 5

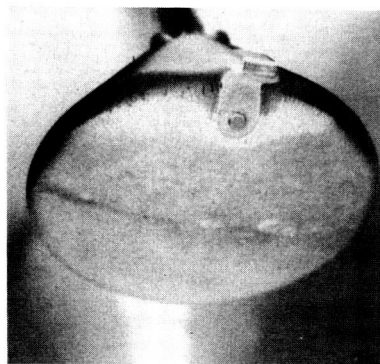


Model 6

(e) $h/h_s = 0.83$.



Model 5

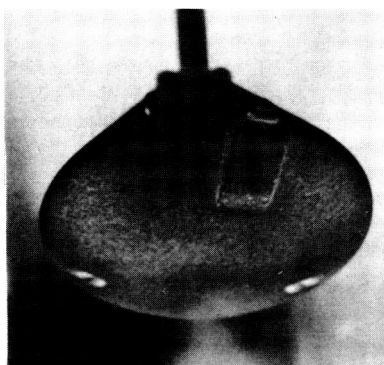


Model 6

(f) $h/h_s = 0.70$.

Figure 22.- Concluded.

L-68-5622

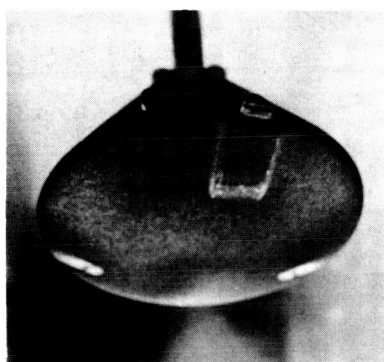


$$R_{\infty,D} = 0.76 \times 10^6$$

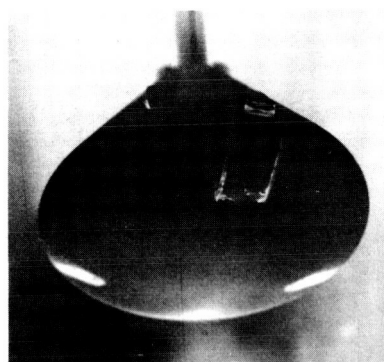


$$R_{\infty,D} = 1.48 \times 10^6$$

(a) $h/h_s = 3.06$.

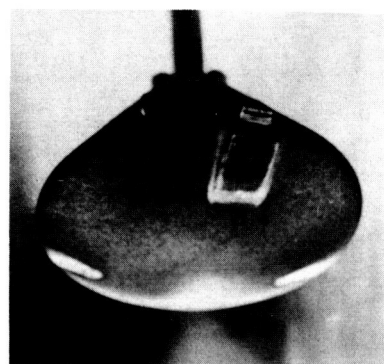


$$R_{\infty,D} = 0.76 \times 10^6$$

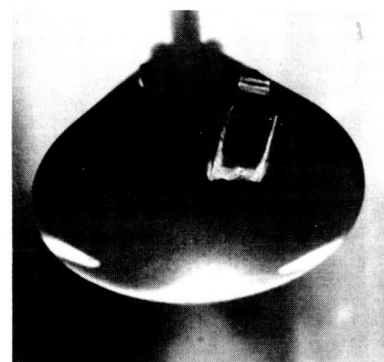


$$R_{\infty,D} = 1.48 \times 10^6$$

(b) $h/h_s = 2.01$.



$$R_{\infty,D} = 0.76 \times 10^6$$

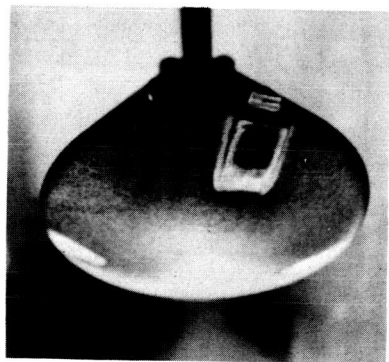


$$R_{\infty,D} = 1.48 \times 10^6$$

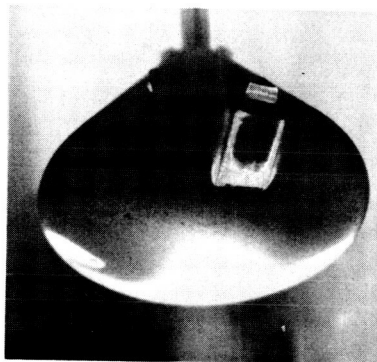
(c) $h/h_s = 1.53$.

Figure 23.- Phase-change patterns for model 1. $\alpha = 26^\circ$.

L-68-5623

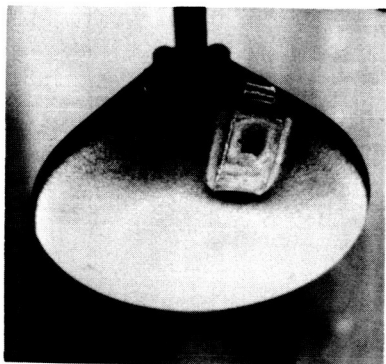


$$R_{\infty,D} = 0.76 \times 10^6$$

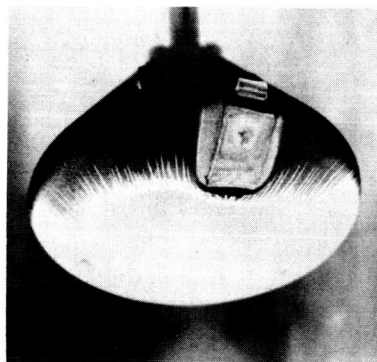


$$R_{\infty,D} = 1.48 \times 10^6$$

(d) $h/h_s = 1.19$.



$$R_{\infty,D} = 0.76 \times 10^6$$

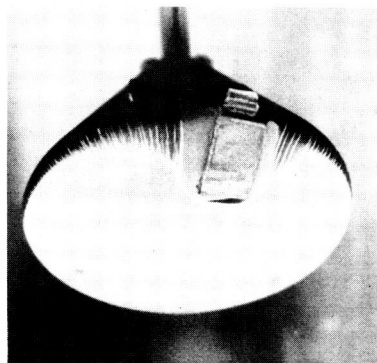


$$R_{\infty,D} = 1.48 \times 10^6$$

(e) $h/h_s = 0.83$.



$$R_{\infty,D} = 0.76 \times 10^6$$



$$R_{\infty,D} = 1.48 \times 10^6$$

(f) $h/h_s = 0.70$.

Figure 23.- Concluded.

L-68-5624

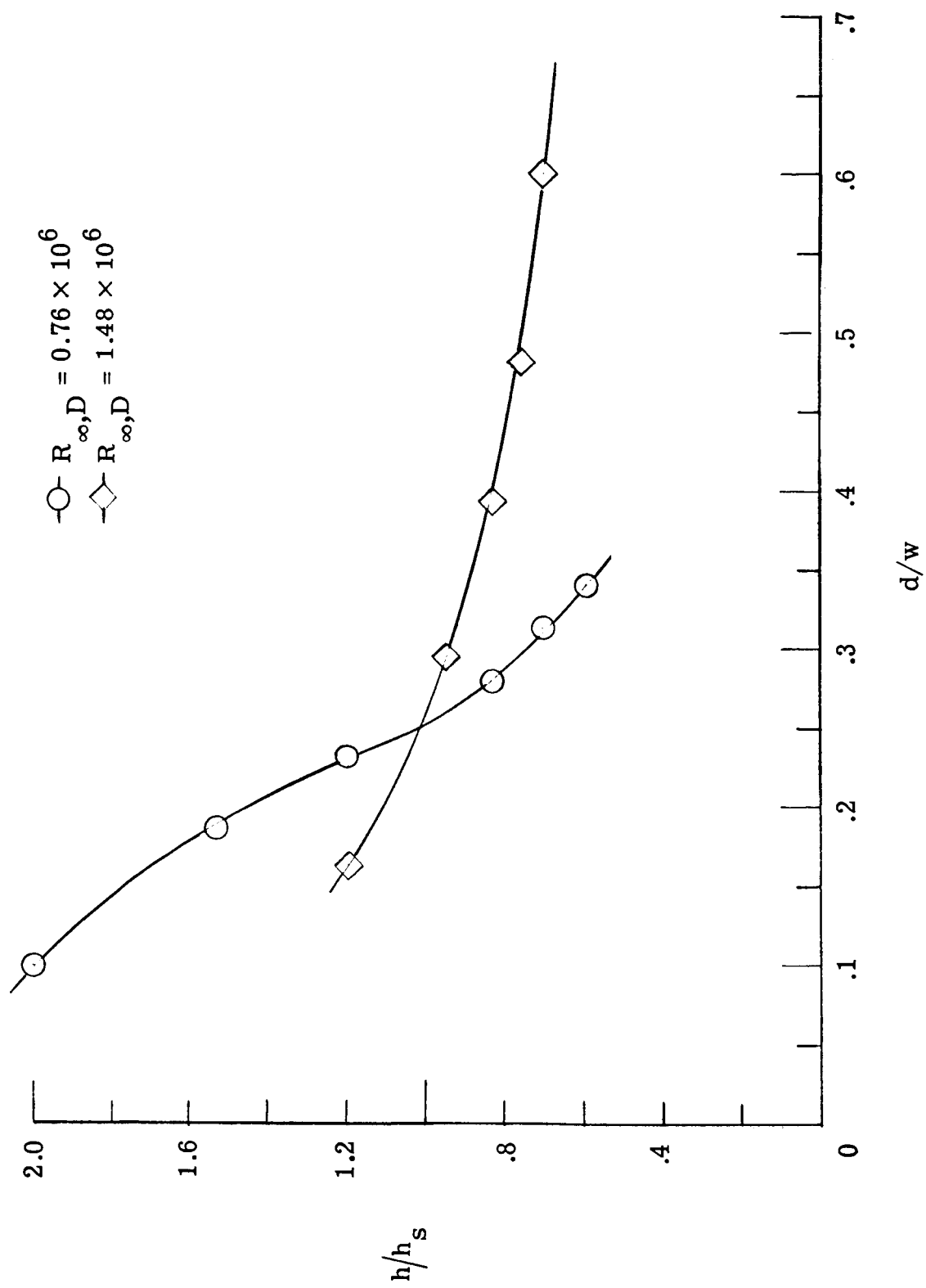
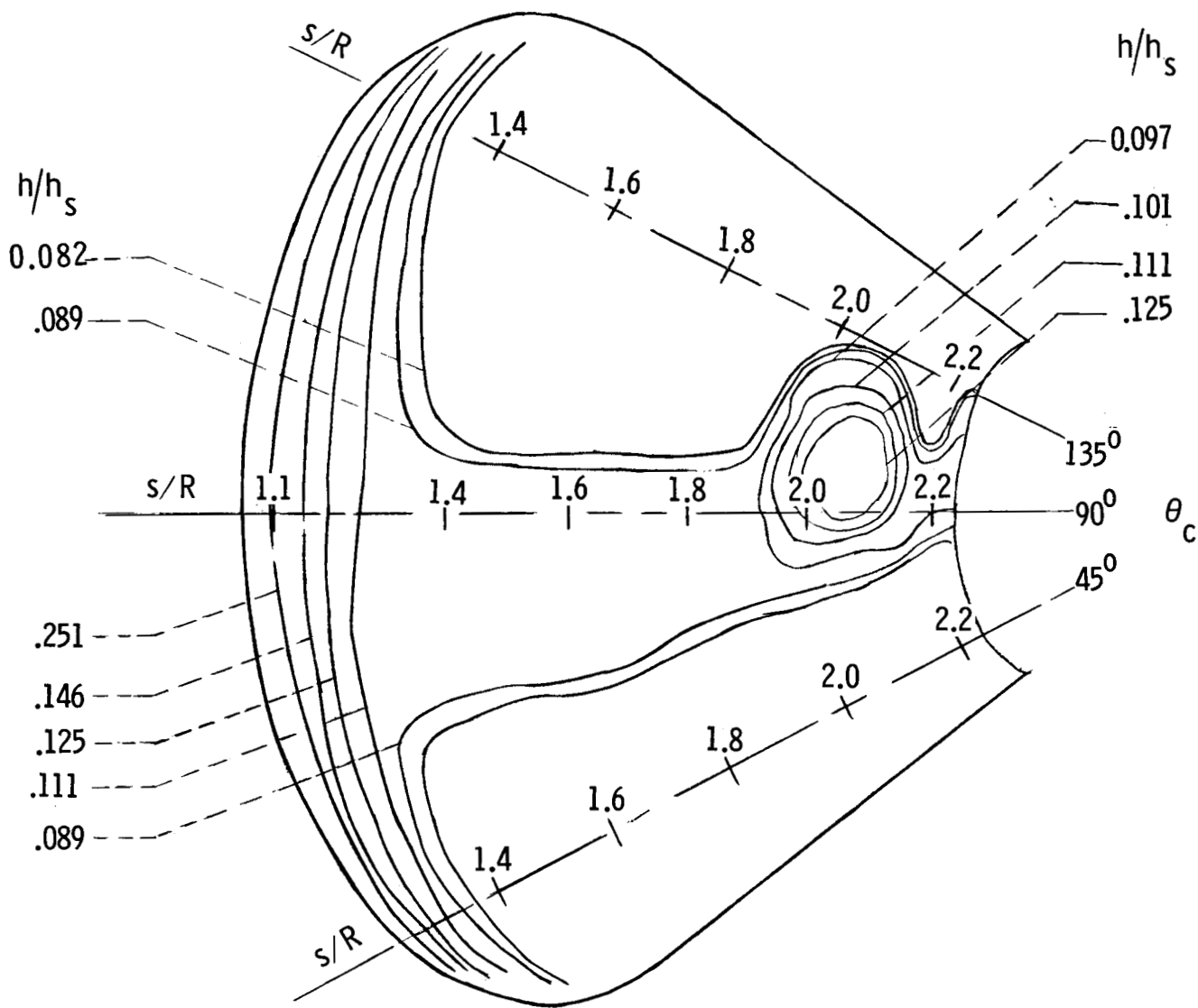
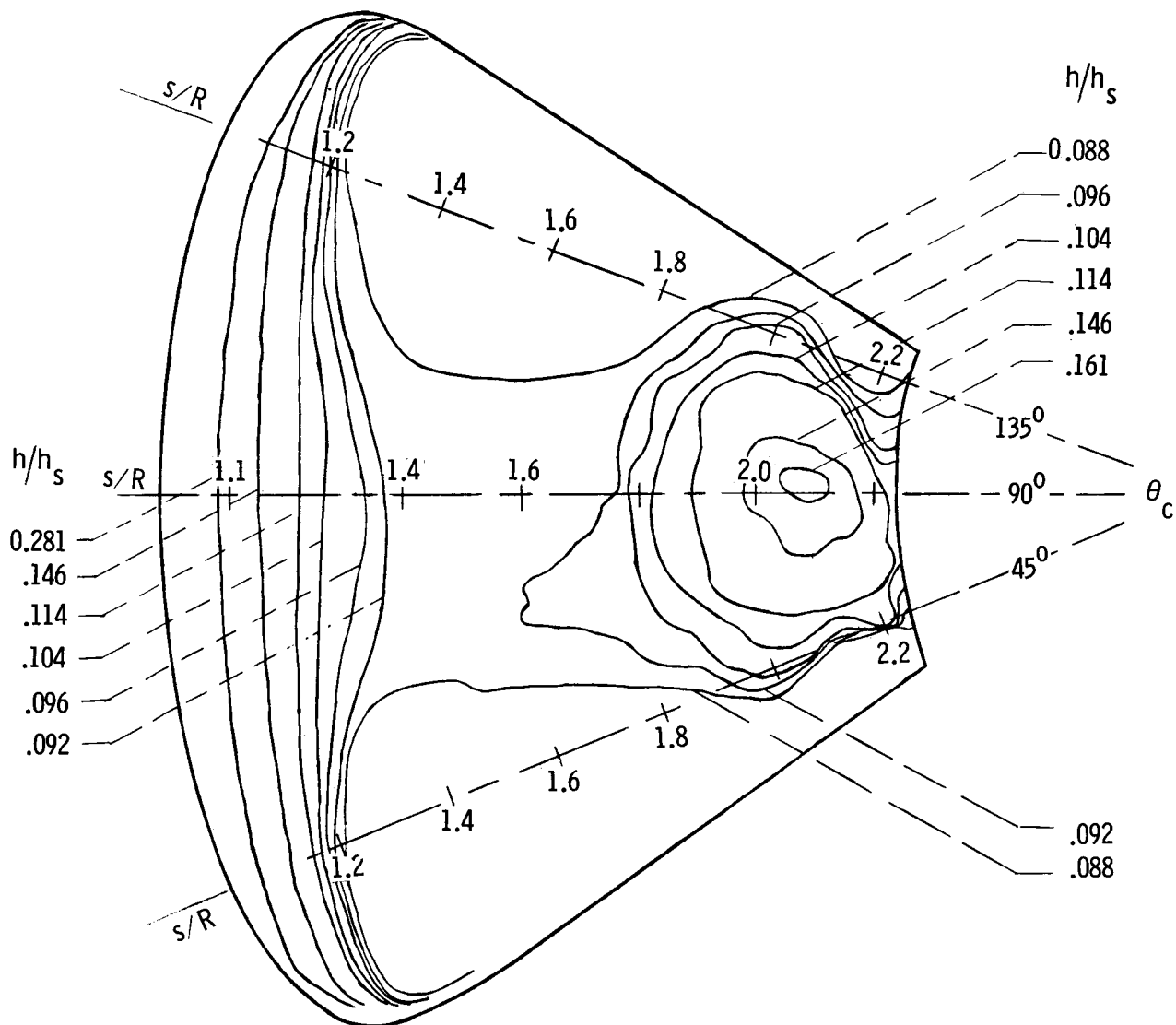


Figure 24.- Effect of Reynolds number on heat-transfer-coefficient distribution in ramp vicinity for model 1.



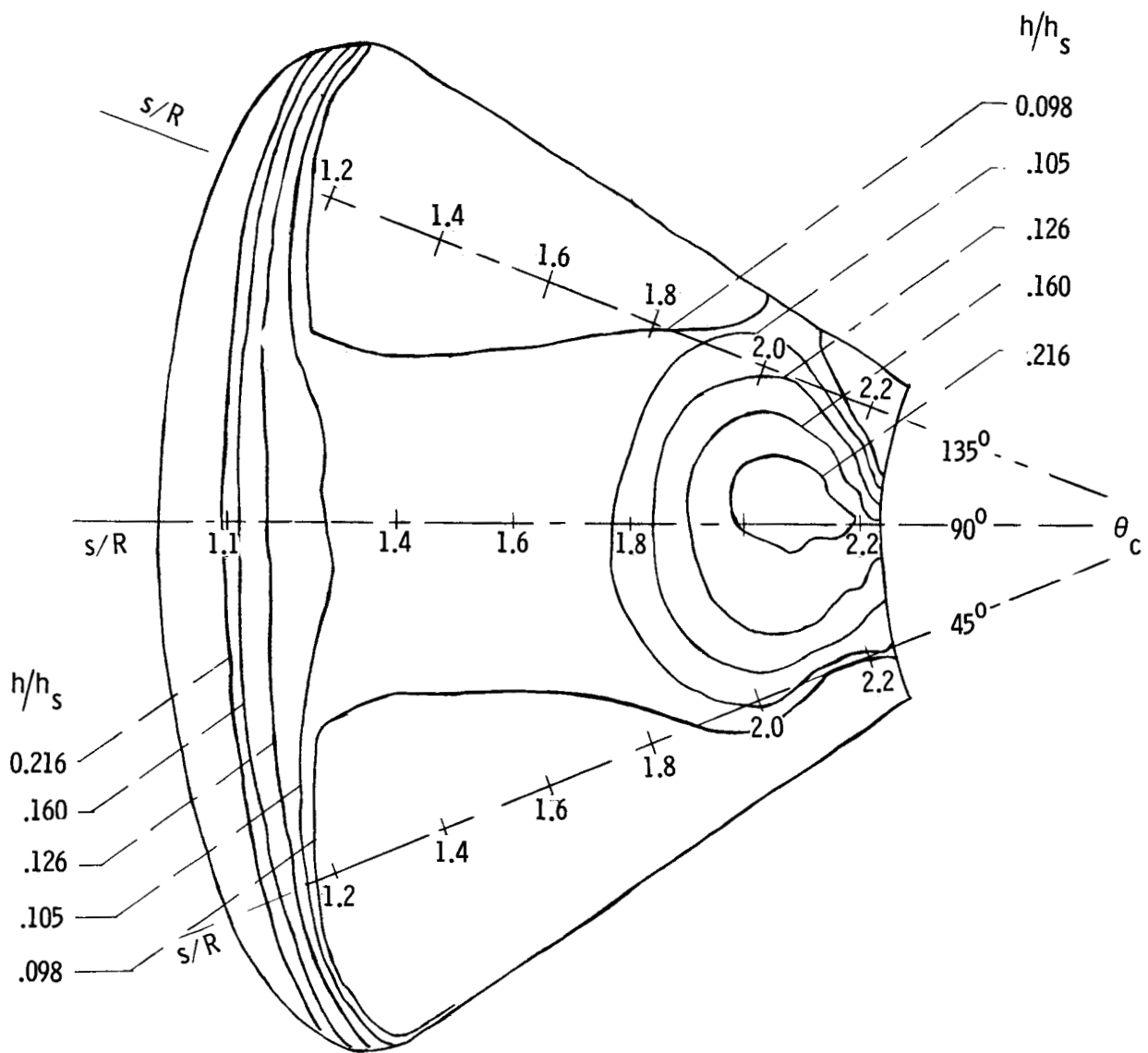
(a) $R_{\infty, D} = 0.20 \times 10^6$; $h_s = 0.942 \times 10^2 \text{ W/m}^2\text{-}^\circ\text{K}$.

Figure 25.- Heat-transfer-coefficient contours on windward side of smooth-model afterbody. Model 8; $\alpha = 22^\circ$.



(b) $R\omega_D = 0.76 \times 10^6$; $h_s = 1.748 \times 10^2 \text{ W/m}^2\text{-}^\circ\text{K}$.

Figure 25.- Continued.



(c) $R_{\infty, D} = 1.48 \times 10^6$; $h_s = 2.432 \times 10^2 \text{ W/m}^2\text{-}^\circ\text{K}$.

Figure 25.- Concluded.

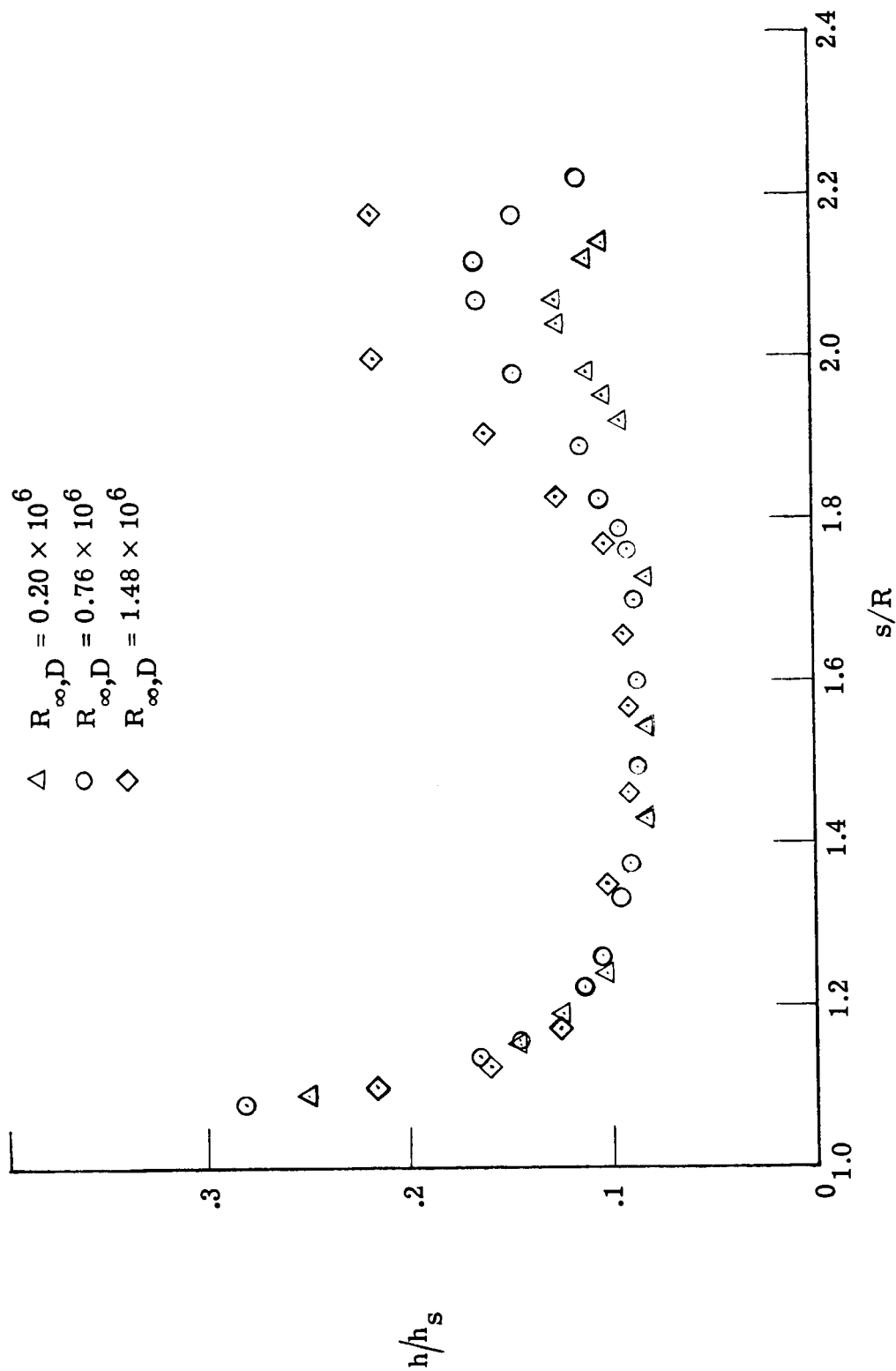
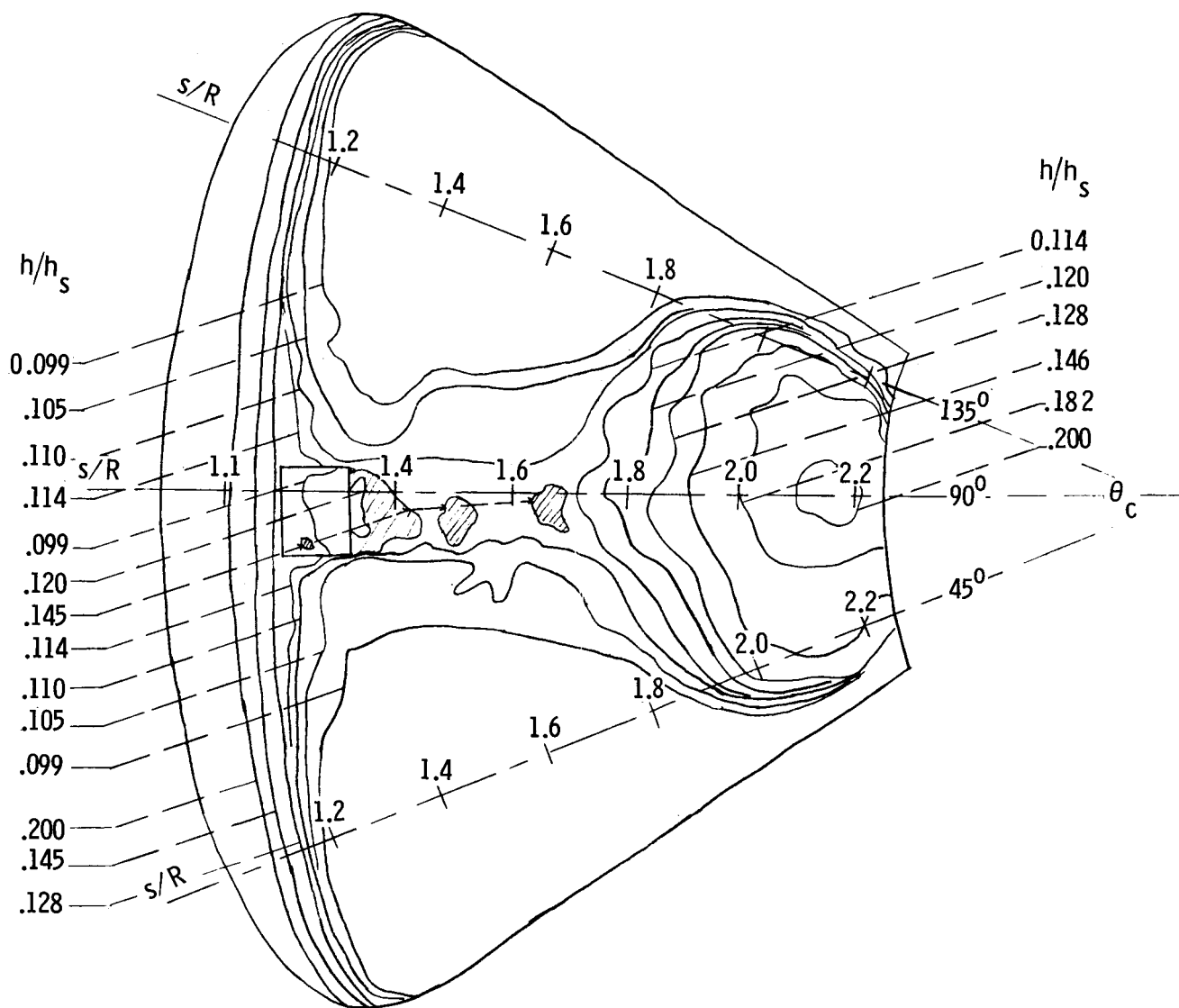
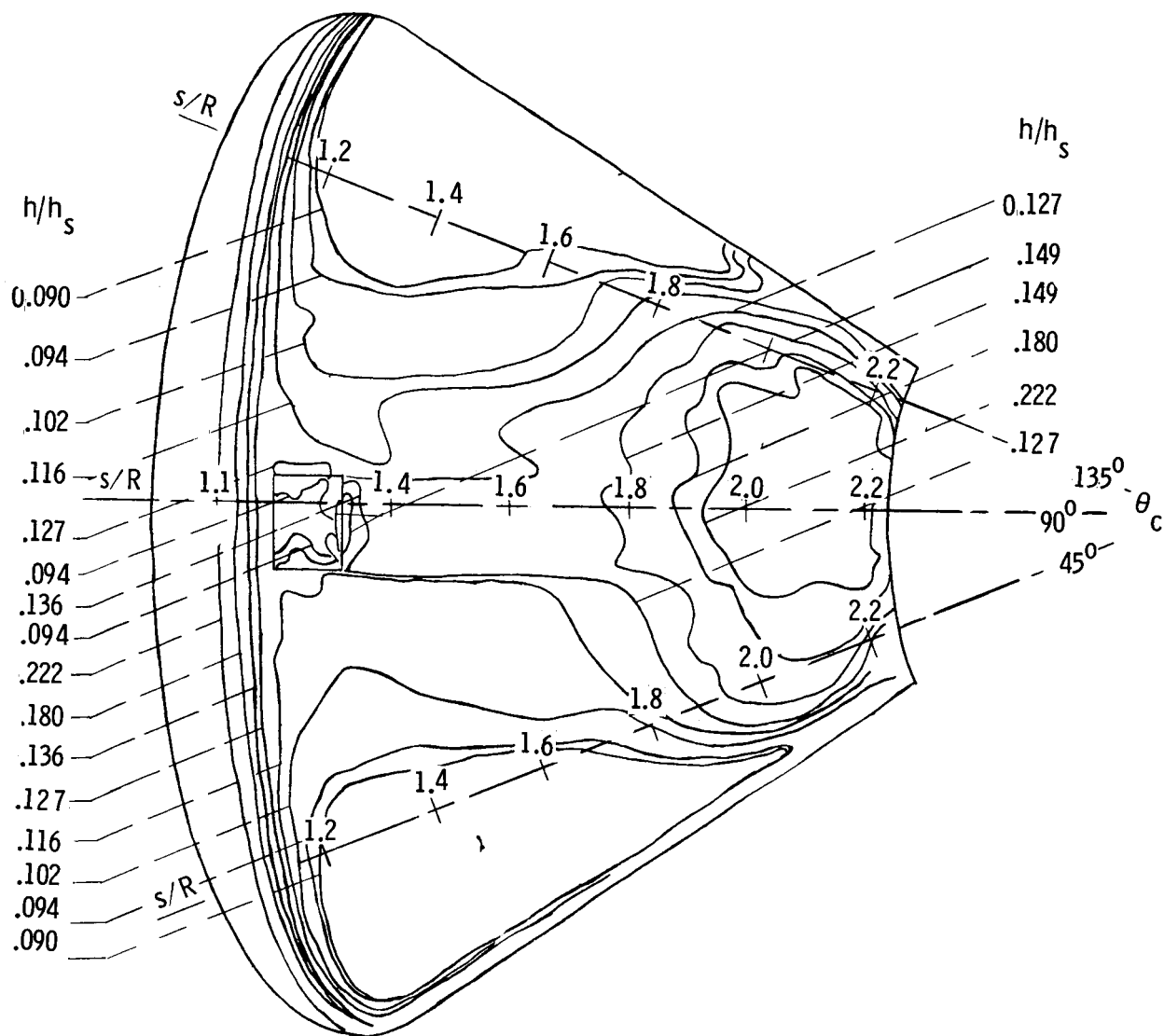


Figure 26.- Heat-transfer ratio along most windward ray of smooth afterbody. Model 8; $\theta_c = 90^\circ$.



(a) $R_{\infty, D} = 0.76 \times 10^6$; $h_s = 1.745 \times 10^2 \text{ W/m}^2\text{-}^\circ\text{K}$.

Figure 27.- Heat-transfer contours on windward side of model 7 afterbody. $\alpha = 22^\circ$.



(b) $R_{\infty, D} = 1.48 \times 10^6$; $h_s = 2.398 \times 10^2 \text{ W/m}^2\text{-}^\circ\text{K}$.

Figure 27.- Concluded.

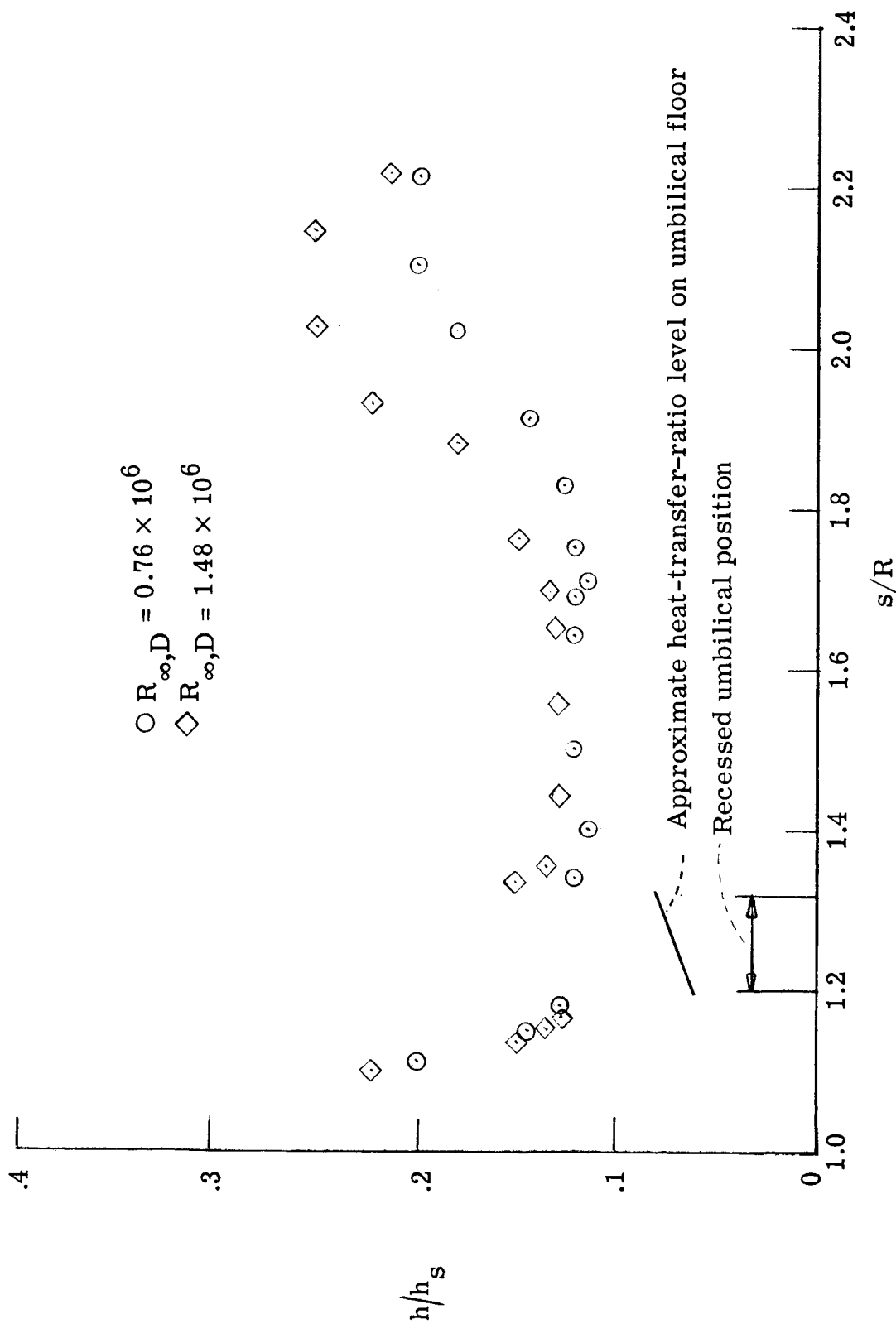


Figure 28.- Heat-transfer-coefficient ratio along most windward ray of model 7 afterbody. $\theta_c = 90^\circ$.

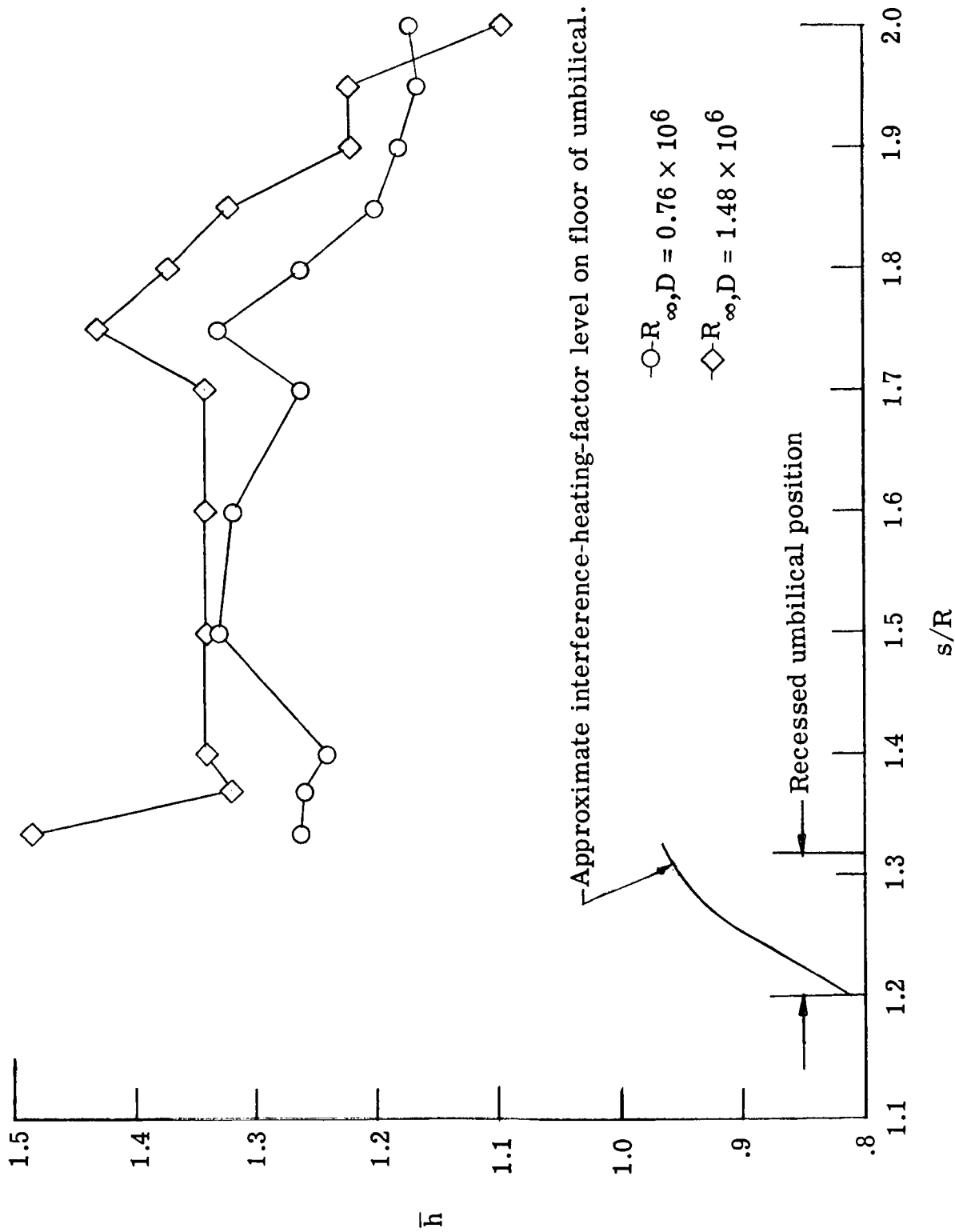


Figure 29.- Interference heating factors along most windward ray of afterbody ($\theta_c = 90^\circ$). $\alpha = 22^\circ$.